Ductility limit prediction for polycrystalline aggregates using a CPFEM-based multiscale framework

J.C. Zhu [a,b], M. Ben Bettaieb [a,c,*], S. Zhou [a,c], F. Abed-Meraim [a,c]

[a] Université de Lorraine, CNRS, Arts et Métiers Institute of Technology, LEM3, Metz F-57070, France
[b] Department of Mechanics, School of Aerospace Engineering, Huazhong University of Science and Technology, Wuhan 430074, China
[c] DAMAS, Laboratory of Excellence on Design of Alloy Metals for low-mAss Structures, Université de Lorraine, France

A B S T R A C T

The ductility of polycrystalline aggregates is usually limited by two main phenomena: plastic strain localization and void coalescence. The goal of this contribution is to develop a new multiscale framework, based on the crystal plasticity finite element method (CPFEM), for the prediction of ductility limits set by these two phenomena for porous and non-porous polycrystalline aggregates. This numerical framework is based on the combination of crystal plasticity constitutive modeling with the periodic homogenization scheme. Within this strategy, the single crystal constitutive modeling follows a finite strain rate-independent approach, where the plastic flow is governed by the classical Schmid law. Thereby, the competition between the two aforementioned phenomena, which limit ductility, is thoroughly analyzed using the bifurcation theory and a strain-based coalescence criterion. To cover a wide range of mechanical states in this analysis, two types of loadings are applied to the studied aggregates: proportional triaxial stress paths and proportional in-plane strain paths. The developed CPFEM-based framework is well suited to account for essential microstructural features: pre-existence of spherical voids, crystallographic and morphological anisotropy, matrix polycrystallinity and interactions between grains and their surrounding medium. Extensive sensitivity studies are performed to analyze the impact of these microstructural features on the ductility limit predictions. The main trends obtained by classical phenomenological frameworks are extended here within the framework of crystal plasticity constitutive modeling.

1. Introduction

Deep understanding of physical phenomena limiting the ductility of thin metal sheets has attracted attention from both computational mechanics and metallurgist communities for several decades. In fact, the insightful knowledge of these phenomena and their accurate modeling play a key role in the safe design of industrial devices and components. Two main phenomena may limit the ductility of thin metal sheets during severe plastic deformations: void coalescence caused by the development of ductile damage, and plastic instability characterized by the onset of localized necking. Ultimate failure is usually the result of the competition between these two phenomena (Tekoğlu et al., 2015). Due to the limited access to fine experimental tools and techniques at the relevant scales and the high cost of experimental testing, extensive investigations have been conducted to develop theoretical and numerical models

* Corresponding author.
E-mail address: Mohamed.BenBettaieb@ensam.eu (M.B. Bettaieb).

able to accurately predict the incipience of plastic instability and damage-induced failure.

Damage evolution inside metal materials has often been modeled by classical phenomenological micromechanics models. These constitutive frameworks, initiated in the seminal work of Gurson (1977), enable to model the growth of a spherical void inside a dense metal matrix. Despite the substantial progress made in the framework of micromechanics-based constitutive descriptions, like the GTN extension performed by Tvergaard and Needleman (Tvergaard and Needleman, 1984), the resulting models remain inaccurate when considering some specific configurations, such as complex loadings or more elaborate constitutive frameworks to characterize the mechanical behavior of the dense matrix. To overcome these drawbacks, several numerical strategies, commonly based on unit cell finite element (FE) computations, have recently been developed. In these approaches, the ductile material is represented by a spatially periodic arrangement of identical unit cells. Consequently, for the constitutive description of such materials, it is sufficient to consider a unique unit cell subjected to relevant boundary conditions that allow effectively reproducing the overall mechanical behavior (classically kinematic or periodic boundary conditions or combination of them). In the current contribution, unit cell computations under periodic boundary conditions (PBCs) are conducted to accurately account for the interactions between the studied unit cell and the neighboring ones. These unit cell computations, based on the periodic homogenization multiscale scheme, are performed within the ABAQUS/Standard FE code. To analyze the impact of initial void and mechanical behavior of the dense matrix on damage-related void coalescence, the unit cell computations are coupled with the strain-based coalescence criterion initiated by Koplik and Needleman (1988).

The ductility of thin metal sheets may also be limited by the initiation of localized necking. To predict this kind of plastic instability, several localized necking criteria have been developed in the literature. In this field, one can quote the bifurcation criterion initially developed by Hill (1952) and rigorously formulated, on the basis of sound theoretical considerations, by Rudnicki and Rice (1975). This criterion detects bifurcation when the acoustic tensor becomes singular, which corresponds to the loss of ellipticity of the partial differential equations governing the associated boundary value problem. Besides its rigorous mathematical foundation, the bifurcation theory does not involve any fitting parameters, such as the initial imperfection size required in the M–K analysis (Marciniak and Kuczynski, 1967). For these reasons, the unit cell approach developed in the present contribution is combined with the bifurcation criterion to predict the occurrence of plastic strain localization in porous and non-porous materials. Because this criterion is founded, in the current study, on the loss of ellipticity of the governing equations at the homogenized level of the unit cell (called hereafter the macroscopic level), the relevant macroscopic tangent modulus needs to be numerically evaluated (Zhu et al., 2020a, 2020b).

Evidently, the predictions performed through unit cell computations are strongly dependent on the constitutive framework used to model the mechanical behavior of the dense matrix and the corresponding material parameters. In the vast majority of previous works, the behavior of the metal matrix has been modeled by phenomenological constitutive descriptions, as in Liu et al. (2016); Reboul et al. (2020); Hosseini et al. (2022); Zhu et al. (2020b). Despite their reliability and their wide application in unit cell computations, phenomenological constitutive frameworks present some conceptual limitations. In fact, classical phenomenological models cannot accurately take into account some key physical features and phenomena, such as crystallographic texture and its evolution, grain morphology, and crystallographic structure. These drawbacks have motivated the use of crystal plasticity models. Unlike phenomenological descriptions, the use of crystal plasticity approaches allows an accurate description of some physical mechanisms and phenomena at the appropriate scale (slip on crystallographic planes, lattice rotation, dislocation motion, grain morphology evolution…). Consequently, several crystal plasticity frameworks have been adopted in unit cell computations to predict void growth and coalescence in porous single crystals or polycrystalline materials (Shang et al., 2020; Christodoulou et al., 2021; Rousselier, 2021). For instance, Yerra et al. (2010) have performed unit cell computations to predict void growth and coalescence in BCC single crystals. According to this study, the authors revealed that the void growth rate is strongly correlated with the initial crystal orientation. It should be noted that several coalescence criteria, based on the Thomason criterion (Thomason, 1990), have been developed and used in Yerra et al. (2010). Numerical predictions based on porous unit cells with an elastoviscoplastic single crystal plasticity model incorporating effects of strain hardening and softening associated with irradiation-induced defects have been performed by Ling et al. (2017). More recently, the void growth in a polycrystalline matrix (made of a large number of single crystals) has been investigated on the basis of unit cell computations by Liu et al. (2021). In the present investigation, the mechanical behavior of porous and non-porous polycrystalline aggregates is studied using the proposed CPFEM approach (CPFE-based unit cell strategy). Unlike all former studies, the mechanical behavior of the constituent single crystals in the proposed approach is modeled by a rate-independent framework. In this formulation, the plastic deformation (at the single crystal scale) is due to the activation of crystallographic slip systems, and the plastic flow obeys the classical Schmid law, which is characterized by the development of vertices on the corresponding yield surface. It is worth noting that the development of such vertices induces destabilizing effects that allow predicting the occurrence of plastic instability in non-porous polycrystalline aggregates at realistic strain levels. In other words, plastic strain localization may be captured by bifurcation analysis in non-porous unit cells when the behavior of the dense matrix is modeled by a rate-independent crystal plasticity theory. This is not the case when the behavior of the matrix material is modeled within a rate-dependent crystal plasticity framework. Thus, the rate-dependent crystal plasticity framework is always coupled with the M–K approach to predict the onset of strain localization (Neil and Agnew, 2009; Signorelli et al., 2009; Serenelli et al., 2010; Serenelli et al., 2011; Schwindt et al., 2015). To the authors' knowledge, rate-independent crystal plasticity framework has not been sufficiently explored in modeling the mechanical behavior of the metal matrix within unit cell computational strategy. Hence, the coupling of the proposed rate-independent CPFEM framework with the bifurcation criterion to study the onset of plastic strain localization represents the most important novelty of the present contribution as compared to previous studies performed by the authors (Zhu et al., 2020a; 2020b).

The competition between plastic strain localization and void coalescence has been studied using phenomenological micromechanics-based frameworks (Nasir et al., 2021). However, the use of unit cell computations to analyze such a competition has seldom been attempted in previous investigations. In this field, readers are referred to Zhu et al. (2020b) who have used the energy-based criterion and the bifurcation approach in conjunction with unit cell computations to elucidate which of the two phenomena occurs first. The latter contribution has demonstrated that strain localization plays a precursor role in the development of void coalescence. In addition, they revealed that the difference in the critical strains at the incipience of localized necking and void coalescence decreases with decreasing the stress triaxiality ratio T, which would imply that the two phenomena could occur simultaneously for sufficiently low triaxiality T. In the present contribution, the competition between these two phenomena is investigated using the developed CPFEM-based approach, and the influence of the initial crystallographic texture on this competition is particularly analyzed. For a wide investigation of the loading state effect on the occurrence of void coalescence and plastic strain localization, two loading configurations are considered in the current unit cell computations: macroscopic proportional triaxial stress paths, where the stress triaxiality ratio T and Lode parameter L are kept constant throughout the loading history, and macroscopic proportional in-plane strain paths, where the in-plane strain-path ratio ρ is kept constant. Only the former loading configuration has been analyzed in the large majority of previous contributions devoted to unit cell computations. The second configuration has not been sufficiently studied using unit cell computations, despite its importance for the '*sheet metal forming*' community. The prediction of FLDs by our unit cell strategy (unit-cell-based periodic homogenization) represents a second novelty of the current contribution, when compared to previous computational methods, such as the FE^2 approach (Klawonn et al., 2020). In the FE^2 approach, numerical simulations of Nakajima or Marciniak tests are conducted using various specimens with different central parallel shafts to achieve the desired strain paths. Each specimen geometry is discretized by finite elements and constrained by boundary conditions similar to those used in FLD experimental determination. A polycrystalline unit cell is assigned to each integration point of the specimen mesh, which is itself discretized by finite elements. The ductility limit is reached when plastic strain localization is observed for the first time in the specimen. This FE^2 approach requires two FE computation levels for each simulation, making it computationally expensive in terms of CPU time. In contrast, the unit-cell strategy proposed in the current contribution involves only one FE computation level, making it more computationally efficient than the FE^2 approach. Additionally, the FLD predictions obtained using the unit-cell strategy depend solely on the mechanical behavior of the considered material, while the FLDs determined by the FE^2 strategy may be influenced by structural effects that can arise due to the specific geometric configuration and external boundary conditions. Hence, the unit-cell strategy seems to be suitable for an accurate prediction of the FLDs.

Another additional novelty of the present contribution concerns the analysis of matrix polycrystallinity effect (due to the use of crystal plasticity theory instead of phenomenological modeling) on plastic strain localization and void coalescence. Despite its importance, this effect has not been investigated in the past, and only few investigations focused on the effect of such matrix polycrystallinity on the void growth rate. In this area, Lebensohn et al. (2013) have revealed that when an isotropic phenomenological model is used for the matrix material, the void growth is only affected by the distance and relative position of the interacting voids. Though, the void behavior is also affected by microstructural effects, which are accounted for within a crystal plasticity modeling framework, such as the influence of the Taylor factor of the crystalline ligaments linking interacting voids. More recently, Liu et al. (2021) have demonstrated that the local heterogeneity of the matrix microstructure, which can only be considered by using a polycrystalline model, retards the void growth. Conversely, the use of traditional phenomenological isotropic constitutive frameworks to model the mechanical behavior of the matrix material leads to overestimation of the void growth rate.

In the present investigation, several numerical simulations are performed to predict the occurrence of failure in non-porous and porous unit cells.

- Non-porous unit cell computations: in these simulations, only plastic strain localization can be predicted (void coalescence is not possible, as the unit cells are non-porous and void nucleation is not considered within the constitutive modeling). The effects of the mechanical state (defined by the triaxiality ratio T and the Lode parameter L, or the strain-path ratio ρ) and the initial crystallographic texture on strain localization occurrence are analyzed.
- Porous unit cell computations: in this case, the predictions are focused on the analysis of the competition between the onset of plastic strain localization predicted by the bifurcation theory and void coalescence determined by the strain-based criterion. The role of the initial crystallographic texture in this competition is specifically highlighted.

The rest of the paper is organized as follows:

✓ In Section 2, the main lines of the periodic homogenization technique, used to determine the overall response of the polycrystalline aggregate, are exposed. Then, the numerical implementation of this technique within ABAQUS/Standard FE code is briefly recalled.
✓ The single crystal constitutive framework is briefly outlined in Section 3. The theoretical framework as well as the numerical implementation of the bifurcation theory are exposed in Section 4.
✓ Section 5 is devoted to the presentation and discussion of the ductility limit predictions obtained by the proposed CPFEM-based strategy.

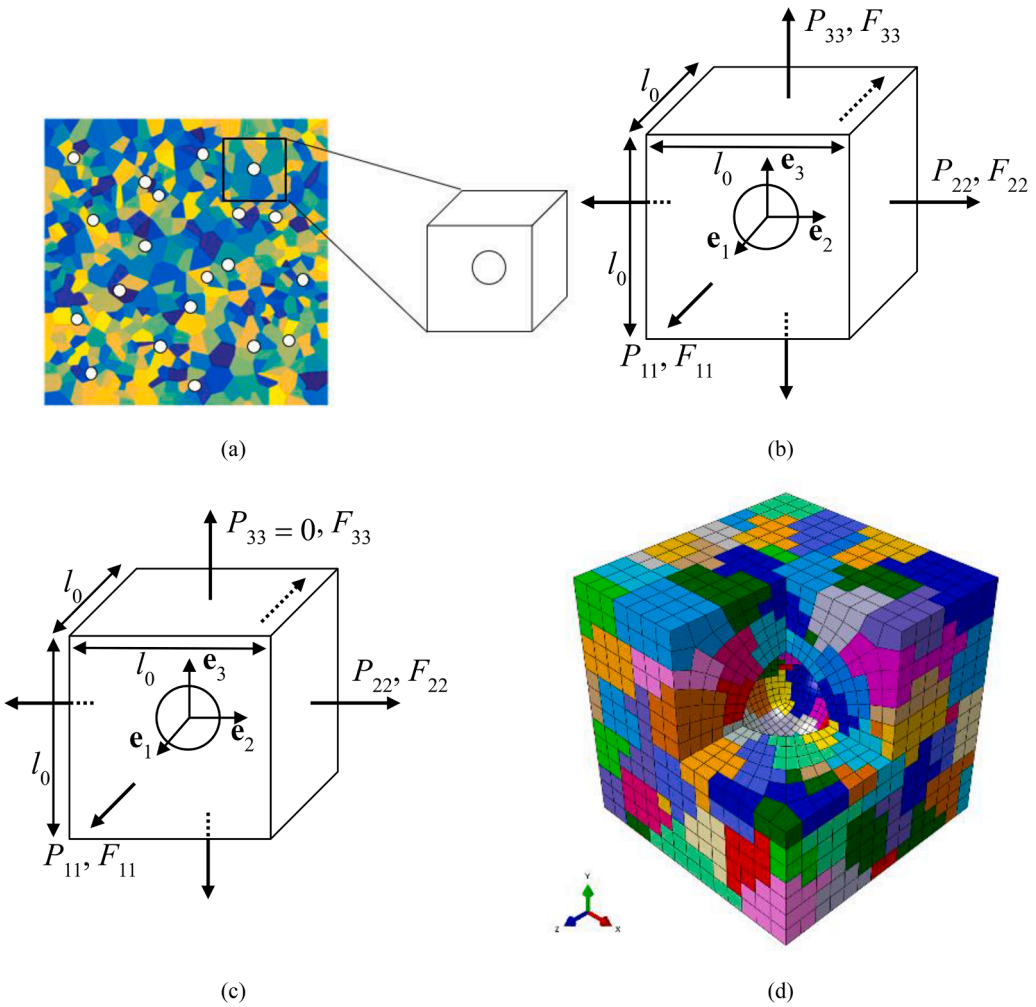

Fig. 1. Porous polycrystalline aggregate: (a) selection of a unit cell from the bulk polycrystalline material; (b) unit cell subjected to a general triaxial macroscopic stress state; (c) unit cell subjected to a biaxial macroscopic plane-stress state; (d) generation of the unit cell by the Voronoi tessellation technique and the corresponding FE mesh.

Conventions, notations and abbreviations

The following notations and conventions are adopted herein:

$\dot{\bullet}$	time derivative of $\bullet$.
${}^{IN}\bullet$	in-plane part of tensor $\bullet$ equal to $\begin{pmatrix} \bullet_{11} \\ \bullet_{21} \end{pmatrix}$ if $\bullet$ is a vector, and $\begin{pmatrix} \bullet_{11} & \bullet_{12} \\ \bullet_{21} & \bullet_{22} \end{pmatrix}$ if $\bullet$ is a second-order tensor, etc.
$\overline{\bullet}$	the transport of $\bullet$ in the intermediate configuration defined by the crystal lattice frame (equal to $\overline{\mathbf{r}}^T \cdot \bullet$ if $\bullet$ is a vector, and $\overline{\mathbf{r}}^T \cdot \bullet \cdot \overline{\mathbf{r}}$ if $\bullet$ is a second-order tensor, with $\overline{\mathbf{r}}$ being the rotation of the crystal lattice frame with respect to the current coordinate system).
$e^{\bullet}$	exponential of field $\bullet$.
$\mathbf{I}_2$	second-rank identity tensor.
$\Delta\bullet$	small perturbation used for the differentiation of field $\bullet$.
T	triaxiality factor equal to the ratio of the hydrostatic stress Σ_h to the von Mises equivalent stress Σ_{eq} ($T = \Sigma_h / \Sigma_{eq}$).
L	Lode parameter, equal to the ratio $(2\Sigma_{22} - \Sigma_{11} - \Sigma_{33})/(\Sigma_{11} - \Sigma_{33})$.
E^B_{eq}	von Mises equvalent limit strain, predicted by the Rice bifurcation criterion (marked by full symbols in the curves).
E^C_{eq}	von Mises equivalent limit strain, predicted by the void coalescence criterion (marked by open symbols in the curves).
Cop.	initial copper crystallographic texture.
Cub.	initial cube crystallographic texture.
Ran.	initial random crystallographic texture.

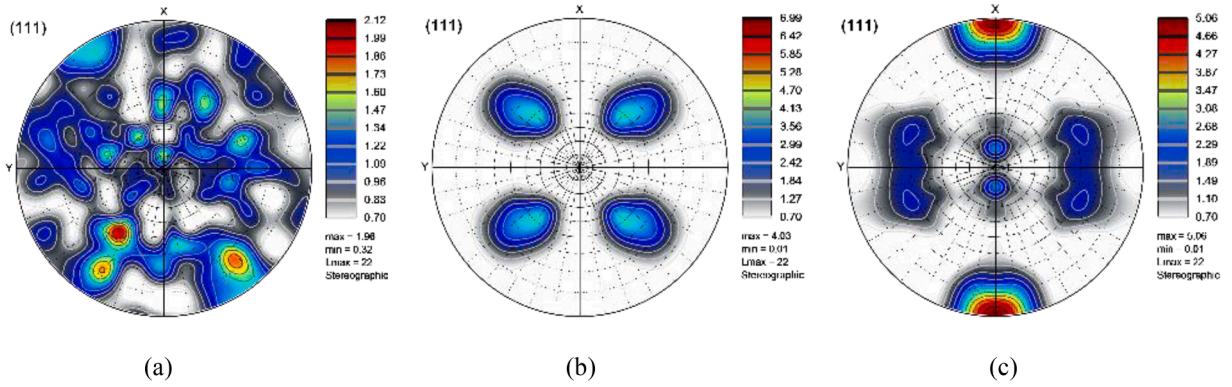

(a) (b) (c)

Fig. 2. Initial crystallographic textures in the form of (111) pole figures: (a) random texture (Ran.); (b) cube texture (Cub.); (c) copper texture (Cop.).

2. Periodic homogenization problem

2.1. Unit cell formulation

The main objective of the current investigation is to develop a numerical strategy, based on the CPFEM, to predict the ductility limits for porous and non-porous polycrystalline metal sheets. Considering the spatial quasi-periodicity of the crystallographic structure in polycrystalline aggregates, and hence of the various mechanical fields, the periodic homogenization scheme turns out to be a good candidate to build this strategy. The first step in the development of this multiscale procedure concerns the definition of a unit cell, which should be sufficiently representative of bulk polycrystalline sheets, as depicted in Fig. 1a. For the computational analysis of the ductility limit of porous aggregates, it is assumed that the void distribution is homogeneous. Thus, a cubic unit cell having a spherical void at its center is considered (Fig. 1a). The studied unit cells are undergoing finite strains, where a total Lagrangian approach is adopted to formulate the periodic homogenization equations and the associated macroscopic boundary conditions. Accordingly, the first Piola–Kirchhoff stress tensor P and the deformation gradient F (see Fig. 1b) are adopted as suitable work-conjugate stress and strain measures. In this investigation, the unit cell, occupying an initial volume $\mathcal{V}_0 = [-l_0/2, l_0/2] \times [-l_0/2, l_0/2] \times [-l_0/2, l_0/2]$, is subjected to either proportional triaxial stressing (triaxial stretching along the three spatial directions with constant macroscopic Cauchy stress ratios) as demonstrated in Fig. 1b, or proportional in-plane strain loading (biaxial stretching along the first and second space directions with constant macroscopic strain-path ratio, while leaving free the third direction) as depicted in Fig. 1c. The unit cell is taken to be composed of 200 FCC grains, on the basis of the grain number sensitivity study provided in Appendix A. The spatial distribution and morphology of these grains are explicitly accounted for using the Voronoi tessellation technique, as shown in Fig. 1d. As clearly shown in Fig. 1d, each grain is discretized by several finite elements, thus allowing the in-grain heterogeneous deformation to be accounted for in the polycrystalline response. This feature cannot be considered if a mean field multiscale scheme (such as the Taylor or self-consistent model) is adopted to derive the unit cell overall behavior. Furthermore, it is assumed that grains are perfectly bound together, with displacement and traction continuity across the grain-boundary interfaces between adjacent grains. The unit cell is discretized, within ABAQUS version 6.14 environment (ABAQUS, 2014), by 5336 C3D20 tri-quadratic isoparametric hexahedral finite elements (Fig. 1d, see Appendix A for the related mesh density sensitivity study). Unless otherwise stated, porous unit cells will be used in Section 5, where the initial void is taken to be spherical and its initial volume fraction f_0 is set to 0.04. This value is in the same order of magnitude as that measured in casting materials (see, e.g., the experimental observations made in Lee, 2020; Lee et al., 2017; Xu et al., 2021). This is a relatively large value chosen so that to perform fast and robust numerical predictions leading to clear trends. Note that, on the one hand, small values of f_0 lead to high computational cost, since the corresponding simulations involve void coalescence. Our objective is to numerically reach the void coalescence stage at a reasonable computational cost, meanwhile to avoid possible numerical problems induced by severe mesh distortion around the void. On the other hand, the selected value of f_0 ensures a distinct separation between strain localization and void calescence, which is the main focus of the present work.

To thoroughly investigate the orientation effect on the ductility limit predictions, three crystallographic textures are systematically used: random, cube component (Euler angles of its ideal texture: $\varphi_1 = \varphi_2 = \Phi = 0°$) and copper component (Euler angles of its ideal texture: $\varphi_1 = 90°$, $\Phi = 35°$, $\varphi_2 = 45°$) textures as defined in Raabe and Rooters (2004). The parameterization of the crystallographic orientation by the Euler angles φ_1, φ_2 and Φ is described by Eq. (26). These initial crystallographic textures will be briefly designated in what follows as 'Ran.', 'Cub.', and 'Cop.', whose spreading angle from their ideal orientation is 15°. The (111) pole figures corresponding to these textures are plotted in Fig. 2 using ATEX software (Beausir and Fundenberger, 2017). For all of the simulations in the present study, the x direction of the unit cell coincides with the x direction marked on the pole figures of textures.

To clearly explain the formulation of the periodic homogenization problem, the two loading configurations will be separately treated: proportional triaxial stress paths in Section 2.2 and proportional in-plane strain paths in Section 2.3.

2.2. Proportional triaxial stress paths

2.2.1. Multiscale equations

The main equations of the periodic homogenization technique, used to determine the overall mechanical behavior of the unit cell undergoing proportional triaxial stress state, are outlined in the following lines:

- The kinematic relation assuming the additive decomposition of the microscopic deformation gradient $\mathbf{f}$ into its macroscopic counterpart $\mathbf{F}$ and a superimposed periodic fluctuation gradient $\mathbf{f}_{per}$, which reflects the heterogeneity of the mechanical behavior induced by the difference in the crystallographic orientation between the constituent grains (crystallographic texture):

$$\mathbf{f} = \mathbf{F} + \mathbf{f}_{per}. \tag{1}$$

The current coordinates $\mathbf{x}$ of a material point are thereby determined by spatial integration of Eq. (1):

$$\mathbf{x} = \mathbf{F} \cdot \mathbf{x}_0 + \mathbf{u}_{per}, \tag{2}$$

where $\mathbf{x}_0$ is the initial coordinate vector of the material point, and $\mathbf{u}_{per}$ is a periodic displacement field.

The time derivative of Eq. (2) enables to obtain the expression of the velocity $\mathbf{v}$:

$$\mathbf{v} = \dot{\mathbf{F}} \cdot \mathbf{x}_0 + \dot{\mathbf{u}}_{per} := \dot{\mathbf{F}} \cdot \mathbf{x}_0 + \mathbf{v}_{per}. \tag{3}$$

- The averaging relations linking the microscopic deformation gradient $\mathbf{f}$ to its macroscopic counterpart $\mathbf{F}$, and the microscopic first Piola–Kirchhoff stress tensor $\mathbf{p}$ to its macroscopic counterpart $\mathbf{P}$ by volume integration over the initial domain $\mathscr{V}_0$:

$$\mathbf{F} = \frac{1}{|\mathscr{V}_0|}\int_{\mathscr{V}_0} \mathbf{f}\, d\mathscr{V}_0 \quad ; \quad \mathbf{P} = \frac{1}{|\mathscr{V}_0|}\int_{\mathscr{V}_0} \mathbf{p}\, d\mathscr{V}_0. \tag{4}$$

Eq. (4) can be equivalently rewritten in its rate form:

$$\dot{\mathbf{F}} = \frac{1}{|\mathscr{V}_0|}\int_{\mathscr{V}_0} \dot{\mathbf{f}}\, d\mathscr{V}_0 \quad ; \quad \dot{\mathbf{P}} = \frac{1}{|\mathscr{V}_0|}\int_{\mathscr{V}_0} \dot{\mathbf{p}}\, d\mathscr{V}_0. \tag{5}$$

- The microscopic static equilibrium equation expressed as a function of $\dot{\mathbf{p}}$ (when body forces are neglected):

$$\mathrm{div}_{\mathbf{x}_0}(\dot{\mathbf{p}}) = 0. \tag{6}$$

- The constitutive equations governing the single crystal mechanical behavior will be presented and adequately solved in Section 3.

2.2.2. Macroscopic loading

In this loading configuration, the unit cell is undergoing a diagonal triaxial macroscopic stress state (see Fig. 1b), i.e., only the diagonal components P_{11}, P_{22}, and P_{33} of the macroscopic stress tensor $\mathbf{P}$ are different from zero (macroscopic shear stresses are neglected). Proportional triaxial stressing requires that the Cauchy stress ratios $\beta_1 = \Sigma_{11}/\Sigma_{33}$ and $\beta_2 = \Sigma_{22}/\Sigma_{33}$ are kept constant during the loading, where Σ_{11}, Σ_{22} and Σ_{33} refer to the diagonal components of the macroscopic Cauchy stress tensor $\mathbf{\Sigma}$.

The hydrostatic stress Σ_h and von Mises equivalent stress Σ_{eq} are thereby represented as functions of stress ratios β_1 and β_2:

$$\Sigma_h = \frac{\beta_1 + \beta_2 + 1}{3}\Sigma_{33} \quad ; \quad \Sigma_{eq} = \frac{1}{\sqrt{2}}\sqrt{(\beta_1 - \beta_2)^2 + (\beta_1 - 1)^2 + (\beta_2 - 1)^2}\,|\Sigma_{33}|. \tag{7}$$

Following the formulations of Liu et al. (2016) and Zhu et al. (2020b), the macroscopic stress triaxiality ratio T and Lode parameter L can be written as functions of the stress ratios β_1 and β_2 by assuming $\Sigma_{11} \geq \Sigma_{22} \geq \Sigma_{33}$:

$$\begin{cases} T = \dfrac{\Sigma_h}{\Sigma_{eq}} = \dfrac{\sqrt{2}(1 + \beta_1 + \beta_2)}{3\sqrt{(1 - \beta_1)^2 + (1 - \beta_2)^2 + (\beta_1 - \beta_2)^2}}\,\mathrm{sgn}(\Sigma_{33}); \\ L = \dfrac{(2\beta_2 - \beta_1 - 1)}{\beta_1 - 1}, -1 \leq L \leq 1. \end{cases} \tag{8}$$

Constant stress ratios β_1 and β_2 during the deformation history result in constant T and L.

2.2.3. Numerical aspects

Periodic homogenization relations (1)–(6) are solved by the FE method. Compared to classical FE problems, the periodic homogenization framework presents two key particularities: the kind of loading to which the unit cell is subjected (as traditionally prescribed, displacement or force components are applied on the structure boundary, and not the components of macroscopic stress or strain tensors), and the periodic boundary conditions applied on the faces $\mathscr{S}_0^{1^-}$, $\mathscr{S}_0^{1^+}$, $\mathscr{S}_0^{2^-}$, $\mathscr{S}_0^{2^+}$, $\mathscr{S}_0^{3^-}$, $\mathscr{S}_0^{3^+}$ defined by the following coordinate components:

$$\begin{array}{l} \mathscr{S}_0^{1^-} : x_{01} = -l_0/2; \mathscr{S}_0^{1^+} : x_{01} = l_0/2 \\ \mathscr{S}_0^{2^-} : x_{02} = -l_0/2; \mathscr{S}_0^{2^+} : x_{02} = l_0/2 \\ \mathscr{S}_0^{3^-} : x_{03} = -l_0/2; \mathscr{S}_0^{3^+} : x_{03} = l_0/2 \end{array}. \tag{9}$$

To simultaneously handle these two particularities in the FE process, the rate form of the virtual power principle is firstly expressed in the absence of body forces:

$$\int_{\mathscr{V}_0} \left[\frac{\partial \delta \mathbf{v}}{\partial \mathbf{x}_0} : \dot{\mathbf{p}} \right] d\mathscr{V}_0 = \int_{\mathscr{S}_0} \delta \mathbf{v} \cdot \dot{\mathbf{t}}_0 d\mathscr{S}_0, \tag{10}$$

where $\mathscr{S}_0$ ($= \mathscr{S}_0^{1^-} \cup \mathscr{S}_0^{1^+} \cup \mathscr{S}_0^{2^-} \cup \mathscr{S}_0^{2^+} \cup \mathscr{S}_0^{3^-} \cup \mathscr{S}_0^{3^+}$) denotes the boundary surface in the initial configuration, and $\dot{\mathbf{t}}_0$ the nominal traction rate prescribed on $\mathscr{S}_0$. Vector $\dot{\mathbf{t}}_0 = \dot{\mathbf{p}} \cdot \vec{\mathbf{n}}_0$, with $\vec{\mathbf{n}}_0$ being the outer normal to the boundary $\mathscr{S}_0$.

To solve Eq. (10), the Hill–Mandel condition is usually used. This condition, proven in a finite strain Lagrangian formulation by De Souza Neto and Feijóo (2010) and Nemat-Nasser (1999), states the incremental internal power equivalence between the micro and macro scales as:

$$\int_{\mathscr{V}_0} \left[\frac{\partial \delta \mathbf{v}}{\partial \mathbf{x}_0} : \dot{\mathbf{p}} \right] d\mathscr{V}_0 = |\mathscr{V}_0| \, \delta \dot{\mathbf{F}} : \dot{\mathbf{P}} \Leftrightarrow \int_{\mathscr{V}_0} \left[\frac{\partial \delta \mathbf{v}}{\partial \mathbf{x}_0} : \dot{\mathbf{p}} \right] d\mathscr{V}_0 - |\mathscr{V}_0| \, \delta \dot{\mathbf{F}} : \dot{\mathbf{P}} = 0. \tag{11}$$

To numerically enforce this equation and hence to apply the macroscopic loading as well as the PBCs, the macroscopic reference point technique is used (Temizer and Wriggers, 2008). This technique suggests to practically consider $\dot{\mathbf{F}}$ as a set of macroscopic degrees of freedom associated with the nodal forces $|\mathscr{V}_0| \, \dot{\mathbf{P}}$. With this general triaxial stress state, three macroscopic reference points are needed to completely apply the components of the macroscopic loading. Further details about the implementation of this technique can be found in Zhu et al. (2020b).

The periodic homogenization problem is solved within ABAQUS/Standard. Constant T and L are applied via the user subroutine multi-point constraints (MPC), which controls the non-linear relations between the macroscopic strains in the three corresponding loading directions. Numerical and technical details corresponding to this implementation can be found in Liu et al. (2016) and Zhu et al. (2020b).

2.3. Proportional in-plane strain paths

2.3.1. Multiscale equations

Under biaxial stretching in the $\vec{\mathbf{e}}_1 - \vec{\mathbf{e}}_2$ plane, the kinematic relation, equivalent to Eq. (1), allows us to relate the in-plane macroscopic deformation gradient ${}^{IN}\mathbf{F}$ to its microscopic counterpart ${}^{IN}\mathbf{f}$ as follows:

$${}^{IN}\mathbf{f} = {}^{IN}\mathbf{F} + {}^{IN}\mathbf{f}_{per}, \tag{12}$$

where ${}^{IN}\mathbf{f}_{per}$ is an in-plane fluctuation gradient that is periodic over the boundaries $\mathscr{S}_0^{1^-} \cup \mathscr{S}_0^{1^+} \cup \mathscr{S}_0^{2^-} \cup \mathscr{S}_0^{2^+}$.

Spatial integration of Eq. (12) leads to the in-plane counterpart of Eq. (2):

$${}^{IN}\mathbf{x} = {}^{IN}\mathbf{F} \cdot {}^{IN}\mathbf{x}_0 + {}^{IN}\mathbf{u}_{per}. \tag{13}$$

The expression of the in-plane velocity ${}^{IN}\mathbf{v}$ can be obtained by taking the time derivative of Eq. (13):

$${}^{IN}\mathbf{v} = {}^{IN}\dot{\mathbf{F}} \cdot {}^{IN}\mathbf{x}_0 + {}^{IN}\mathbf{v}_{per}. \tag{14}$$

The other equations exposed in Section 2.2.1 (namely, Eqs. (4)–(6)) remain valid for in-plane biaxial stretching.

2.3.2. Macroscopic loading

The macroscopic fields characterizing this in-plane biaxial stretching are defined as:

$$\mathbf{F} = \begin{pmatrix} F_{11} & 0 & \square \\ 0 & F_{22} & \square \\ \square & \square & \square \end{pmatrix} \quad ; \quad \mathbf{P} = \begin{pmatrix} \square & \square & 0 \\ \square & \square & 0 \\ 0 & 0 & 0 \end{pmatrix}, \tag{15}$$

where components '$\square$' are unknown and should be obtained by FE computations. Then, the macroscopic loading is imposed on the faces normal to the 1 ($x_{01} = \pm l_0/2$) and 2 ($x_{02} = \pm l_0/2$) directions. On the other hand, faces normal to the 3 direction are free (see

Fig. 1c).

As traditionally followed in the FLD predictions, the components F_{11} and F_{22} are defined as functions of the strain-path ratio ρ (varying between $-1/2$ and 1) and the major strain component E_{11}:

$$F_{11} = e^{E_{11}} \quad ; \quad F_{22} = e^{E_{22}} \quad \text{with} \quad E_{22} = \rho E_{11}. \tag{16}$$

2.3.3. Numerical aspects

The periodic homogenization problem defined by Eqs. (4)–(6), (15)–(16) will be solved by the FE method. As in the triaxial stressing case (see, Section 2.2.3), the solution method of this homogenization problem is based on the Hill–Mandel condition given by Eq. (11). The validity of this condition under macroscopic plane-stress assumption is proven in the subsequent developments. Following the decomposition of the whole boundary of the unit cell $\mathscr{S}_0$ into six faces, the right-hand side of Eq. (10) could be expanded as:

$$\int_{\mathscr{S}_0} \delta\mathbf{v}\cdot\dot{\mathbf{t}}_0\, d\mathscr{S}_0 = \int_{\mathscr{S}_0^{1^-}\cup\mathscr{S}_0^{1^+}\cup\mathscr{S}_0^{2^-}\cup\mathscr{S}_0^{2^+}} \delta\mathbf{v}\cdot\dot{\mathbf{t}}_0\, d\mathscr{S}_0 + \int_{\mathscr{S}_0^{3^-}\cup\mathscr{S}_0^{3^+}} \delta\mathbf{v}\cdot\dot{\mathbf{t}}_0\, d\mathscr{S}_0. \tag{17}$$

Taking into account the macroscopic boundary conditions given by Eq. (15), one can easily deduce that the traction vector $\dot{\mathbf{t}}_0$ is equal to $\overrightarrow{\mathbf{0}}$ over faces $\mathscr{S}_0^{3^-}$ and $\mathscr{S}_0^{3^+}$. Hence, $\int_{\mathscr{S}_0^{3^-}\cup\mathscr{S}_0^{3^+}} \delta\mathbf{v}\cdot\dot{\mathbf{t}}_0\, d\mathscr{S}_0$ is equal to 0. Moreover, the third component of $\dot{\mathbf{t}}_0$ is equal to 0 over faces $\mathscr{S}_0^{1^-}, \mathscr{S}_0^{1^+}, \mathscr{S}_0^{2^-}$ and $\mathscr{S}_0^{2^+}$. Then, $\delta\mathbf{v}\cdot\dot{\mathbf{t}}_0$ reduces to ${}^{IN}\delta\mathbf{v}\cdot{}^{IN}\dot{\mathbf{t}}_0$ over $\mathscr{S}_0^{1^-}\cup\mathscr{S}_0^{1^+}\cup\mathscr{S}_0^{2^-}\cup\mathscr{S}_0^{2^+}$. Consequently, Eq. (17) is reduced to the following form:

$$\int_{\mathscr{S}_0} \delta\mathbf{v}\cdot\dot{\mathbf{t}}_0 d\mathscr{S}_0 = \int_{\mathscr{S}_0} {}^{IN}\delta\mathbf{v}\cdot{}^{IN}\dot{\mathbf{t}}_0\, d\mathscr{S}_0. \tag{18}$$

Hence, Eq. (10) can be transformed as:

$$\int_{\mathscr{V}_0}\left[\frac{\partial\delta\mathbf{v}}{\partial\mathbf{x}_0}:\dot{\mathbf{p}}\right]d\mathscr{V}_0 = \int_{\mathscr{S}_0}\delta\mathbf{v}\cdot\dot{\mathbf{t}}_0 d\mathscr{S}_0 = \int_{\mathscr{S}_0}{}^{IN}\delta\mathbf{v}\cdot{}^{IN}\dot{\mathbf{t}}_0\, d\mathscr{S}_0 = \int_{\mathscr{V}_0}\left[\frac{\partial{}^{IN}\delta\mathbf{v}}{\partial\mathbf{x}_0}:{}^{IN}\dot{\mathbf{p}}\right]d\mathscr{V}_0. \tag{19}$$

Using Eq. (14), the right-hand side of Eq. (19) can be recast as:

$$\begin{aligned}&\int_{\mathscr{V}_0}\left[\frac{\partial{}^{IN}\delta\mathbf{v}}{\partial\mathbf{x}_0}:{}^{IN}\dot{\mathbf{p}}\right]d\mathscr{V}_0 = \int_{\mathscr{V}_0}\left[\left({}^{IN}\delta\dot{\mathbf{F}}+\frac{\partial{}^{IN}\delta\mathbf{v}_{per}}{\partial\mathbf{x}_0}\right):{}^{IN}\dot{\mathbf{p}}\right]d\mathscr{V}_0\\ &= |\mathscr{V}_0|{}^{IN}\delta\dot{\mathbf{F}}:{}^{IN}\dot{\mathbf{P}}+\int_{\mathscr{V}_0}\frac{\partial{}^{IN}\delta\mathbf{v}_{per}}{\partial\mathbf{x}_0}:{}^{IN}\dot{\mathbf{p}}d\mathscr{V}_0 = |\mathscr{V}_0|{}^{IN}\delta\dot{\mathbf{F}}:{}^{IN}\dot{\mathbf{P}}+\int_{\mathscr{S}_0^{1^-}\cup\mathscr{S}_0^{1^+}\cup\mathscr{S}_0^{2^-}\cup\mathscr{S}_0^{2^+}}{}^{IN}\delta\mathbf{v}_{per}.{}^{IN}\dot{\mathbf{t}}_0\, d\mathscr{S}_0.\end{aligned} \tag{20}$$

The periodicity of vector ${}^{IN}\delta\mathbf{v}_{per}$ and the anti-periodicity of vector ${}^{IN}\dot{\mathbf{t}}_0$ over the set of faces $\mathscr{S}_0^{1^-}\cup\mathscr{S}_0^{1^+}\cup\mathscr{S}_0^{2^-}\cup\mathscr{S}_0^{2^+}$ lead to the following boundary integral constraint:

$$\int_{\mathscr{S}_0^{1^-}\cup\mathscr{S}_0^{1^+}\cup\mathscr{S}_0^{2^-}\cup\mathscr{S}_0^{2^+}}{}^{IN}\delta\mathbf{v}_{per}.{}^{IN}\dot{\mathbf{t}}_0\, d\mathscr{S}_0 = 0. \tag{21}$$

Considering Eqs. (19), (20) and (21), the Hill–Mandel condition is validated for the macroscopic plane-stress state:

$$\int_{\mathscr{V}_0}\left[\frac{\partial\delta\mathbf{v}}{\partial\mathbf{x}_0}:\dot{\mathbf{p}}\right]d\mathscr{V}_0 = |\mathscr{V}_0|{}^{IN}\delta\dot{\mathbf{F}}:{}^{IN}\dot{\mathbf{P}}. \tag{22}$$

To apply the macroscopic biaxial stretching in combination with the periodic boundary conditions, two macroscopic reference points are required (see Lejeunes and Bourgeois, 2011). Hence, the in-plane components of $\mathbf{F}$, which define the proportional in-plane strain path (see Eq. (16)), can be easily applied through the displacements of the two reference points.

3. Single crystal constitutive equations

At the microscopic scale, each integration point of the mesh of the unit cell represents a single crystal (see Fig. 1d). Besides, each grain is constituted by a number of single crystals that initially have the same crystallographic orientation. To completely solve the periodic homogenization problem presented in Section 2, the single crystal constitutive framework should be completely formulated and solved. This is the major goal of the current section. These constitutive equations are formulated in a 3D general framework regardless of the studied loading state (i.e., triaxial stress or biaxial strain states).

As a starting point, the microscopic velocity gradient $\mathbf{g}$ is linked to the microscopic deformation gradient $\mathbf{f}$ as follows:

$$\mathbf{g} = \dot{\mathbf{f}}\cdot\mathbf{f}^{-1}, \tag{23}$$

where $\mathbf{f}$ is determined at each integration point by the FE computation.

As stated earlier, the single crystal behavior is assumed to be elasto-plastic. Hence, $\mathbf{f}$ can be multiplicatively decomposed into elastic and plastic parts, denoted respectively $\mathbf{f}^e$ and $\mathbf{f}^p$:

$$\mathbf{f} = \mathbf{f}^e \cdot \mathbf{f}^p.$$

The elastic part $\mathbf{f}^e$ may in turn be partitioned into a symmetric stretching tensor $\mathbf{v}^e$ and a rotation $\bar{\mathbf{r}}$:

$$\mathbf{f}^e = \mathbf{v}^e \cdot \bar{\mathbf{r}}. \tag{25}$$

The rotation tensor $\bar{\mathbf{r}}$ defines the orientation of the crystallographic lattice with respect to the current microscopic coordinate system. This rotation is parameterized by the Euler angles φ_1, φ_2 and Φ (based on the Bunge convention), as shown by the following matrix formulation:

$$\bar{\mathbf{r}} = \begin{bmatrix} \cos\varphi_1 \cos\varphi_2 - \sin\varphi_1 \sin\varphi_2 \cos\Phi & \sin\varphi_1 \cos\varphi_2 + \cos\varphi_1 \sin\varphi_2 \cos\Phi & \sin\varphi_2 \sin\Phi \\ -\cos\varphi_1 \sin\varphi_2 - \sin\varphi_1 \cos\varphi_2 \cos\Phi & -\sin\varphi_1 \sin\varphi_2 + \cos\varphi_1 \cos\varphi_2 \cos\Phi & \cos\varphi_2 \sin\Phi \\ \sin\varphi_1 \sin\Phi & -\cos\varphi_1 \sin\Phi & \cos\Phi \end{bmatrix}. \tag{26}$$

The combination of Eqs. (23), (24), and (25) yields:

$$\begin{aligned} \mathbf{g} &= \dot{\mathbf{f}} \cdot \mathbf{f}^{-1} = \dot{\mathbf{f}}^{\mathrm{e}} \cdot \mathbf{f}^{\mathrm{e}-1} + \mathbf{f}^{\mathrm{e}} \cdot \dot{\mathbf{f}}^{\mathrm{p}} \cdot \mathbf{f}^{\mathrm{p}-1} \cdot \mathbf{f}^{\mathrm{e}-1} \\ &= \dot{\mathbf{v}}^{\mathrm{e}} \cdot \mathbf{v}^{\mathrm{e}-1} + \mathbf{v}^{\mathrm{e}} \cdot \dot{\bar{\mathbf{r}}} \cdot \bar{\mathbf{r}}^{\mathrm{T}} \cdot \mathbf{v}^{\mathrm{e}-1} + \mathbf{v}^{\mathrm{e}} \cdot \bar{\mathbf{r}} \cdot \dot{\mathbf{f}}^{\mathrm{p}} \cdot \mathbf{f}^{\mathrm{p}-1} \cdot \bar{\mathbf{r}}^{\mathrm{T}} \cdot \mathbf{v}^{\mathrm{e}-1}. \end{aligned} \tag{27}$$

As for the majority of metallic materials, the elastic deformation is assumed to be very small compared to unity (i.e., $\mathbf{v}^e \approx \mathbf{I}_2$). Accordingly, Eq. (27) can be simplified as:

$$\mathbf{g} = \dot{\mathbf{v}}^e + \dot{\bar{\mathbf{r}}} \cdot \bar{\mathbf{r}}^T + \bar{\mathbf{r}} \cdot \dot{\mathbf{f}}^p \cdot \mathbf{f}^{p-1} \cdot \bar{\mathbf{r}}^T. \tag{28}$$

The velocity gradient $\mathbf{g}$ can be additively decomposed into its symmetric part $\mathbf{d}$ and skew-symmetric part $\mathbf{w}$:

$$\mathbf{g} = \mathbf{d} + \mathbf{w} \quad \text{where} \quad \mathbf{d} = \frac{1}{2}\left(\mathbf{g} + \mathbf{g}^T\right) \quad \text{and} \quad \mathbf{w} = \frac{1}{2}\left(\mathbf{g} - \mathbf{g}^T\right), \tag{29}$$

which are themselves decomposed into elastic and plastic parts $\mathbf{d}^e$, $\mathbf{d}^p$, $\mathbf{w}^e$, and $\mathbf{w}^p$:

$$\begin{aligned} &\mathbf{d} = \mathbf{d}^e + \mathbf{d}^p \quad ; \quad \mathbf{w} = \mathbf{w}^e + \mathbf{w}^p; \\ &\mathbf{d}^e = \dot{\mathbf{v}}^e \quad ; \quad \mathbf{d}^p = \frac{1}{2}\bar{\mathbf{r}} \cdot \left(\dot{\mathbf{f}}^p \cdot \mathbf{f}^{p-1} + \left(\dot{\mathbf{f}}^p \cdot \mathbf{f}^{p-1}\right)^T\right) \cdot \bar{\mathbf{r}}^T; \cdot \bar{\mathbf{r}}^T \quad ; \quad \mathbf{w}^p = \frac{1}{2}\bar{\mathbf{r}} \cdot \left(\dot{\mathbf{f}}^p \cdot \mathbf{f}^{p-1} - \left(\dot{\mathbf{f}}^p \cdot \mathbf{f}^{p-1}\right)^T\right) \cdot \bar{\mathbf{r}}^T. \\ &\qquad\qquad \mathbf{w}^e = \dot{\bar{\mathbf{r}}} \end{aligned} \tag{30}$$

By assuming that plastic deformation is exclusively induced by slip on the crystallographic slip systems, tensor $\bar{\mathbf{r}} \cdot \dot{\mathbf{f}}^p \cdot \mathbf{f}^{p-1} \cdot \bar{\mathbf{r}}^T$ can be expressed as:

$$\bar{\mathbf{r}} \cdot \dot{\mathbf{f}}^p \cdot \mathbf{f}^{p-1} \cdot \bar{\mathbf{r}}^T = \sum_{\alpha=1}^{12} \dot{\gamma}^\alpha \mathbf{M}^\alpha, \tag{31}$$

where:

- $\dot{\gamma}^\alpha$ refers to the algebraic value of the slip rate of the α^{th} slip system.
- $\mathbf{M}^\alpha$ designates the Schmid tensor of slip system α, equal to the tensor product of the slip direction vector $\vec{\mathbf{m}}^\alpha$ and the vector normal to the slip plane $\vec{\mathbf{n}}^\alpha$:

$$\mathbf{M}^\alpha = \vec{\mathbf{m}}^\alpha \otimes \vec{\mathbf{n}}^\alpha. \tag{32}$$

For evident practical reasons, and in order to handle only positive values of slip rates in the numerical implementation, it is more convenient to break each slip system into two opposite pseudo-slip systems $(\vec{\mathbf{m}}^\alpha, \vec{\mathbf{n}}^\alpha)$ and $(-\vec{\mathbf{m}}^\alpha, \vec{\mathbf{n}}^\alpha)$, numbered as α and $\alpha + 12$, respectively. With this decomposition, Eq. (31) is recast as:

$$\bar{\mathbf{r}} \cdot \dot{\mathbf{f}}^p \cdot \mathbf{f}^{p-1} \cdot \bar{\mathbf{r}}^T = \sum_{\alpha=1}^{24} \dot{\gamma}^\alpha \mathbf{M}^\alpha \quad \text{with} \quad \dot{\gamma}^\alpha \geq 0. \tag{33}$$

Using Eq. (33), the plastic strain rate $\mathbf{d}^p$ and plastic spin $\mathbf{w}^p$, introduced in Eq. (30), can be expressed as functions of the symmetric and skew-symmetric parts $\mathbf{R}^\alpha$ and $\mathbf{S}^\alpha$ of the Schmid tensor $\mathbf{M}^\alpha$:

$$\mathbf{d}^p = \sum_{\alpha=1}^{24} \dot{\gamma}^\alpha \mathbf{R}^\alpha \quad ; \quad \mathbf{w}^p = \sum_{\alpha=1}^{24} \dot{\gamma}^\alpha \mathbf{S}^\alpha. \tag{34}$$

The list of vectors $\vec{\mathbf{m}}_0^\alpha$ and $\vec{\mathbf{n}}_0^\alpha$ for FCC single crystals can be found in Akpama et al. (2017).

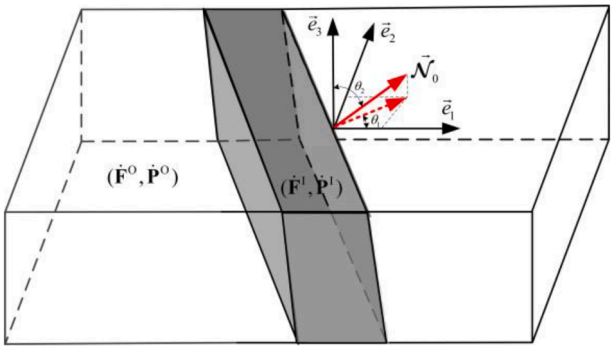

Fig. 3. Illustration of the jump of mechanical fields of interest across the band plane.

To fulfill the objectivity principle, we introduce the lattice co-rotational derivative $\boldsymbol{\sigma}^{\nabla}$ of the Cauchy stress tensor related to the time derivative $\dot{\boldsymbol{\sigma}}$ by the following relation:

$$\boldsymbol{\sigma}^{\nabla} = \dot{\boldsymbol{\sigma}} - \mathbf{w}^e \cdot \boldsymbol{\sigma} + \boldsymbol{\sigma} \cdot \mathbf{w}^e. \tag{35}$$

Elasticity is assumed to be linear and isotropic and is given by the Hooke law:

$$\dot{\boldsymbol{\sigma}} = \boldsymbol{l}^e : \mathbf{d}^e, \tag{36}$$

where $\boldsymbol{l}^e$ is the fourth-order elastic stiffness tensor.

For rate-independent behavior, the plastic flow is defined by the Schmid law, which states that slip system α is activated (i.e. $\dot{\gamma}^\alpha \geq 0$) when the resolved shear stress τ^α reaches a critical value τ_c^α:

$$\forall \alpha = 1, ..., 24: \quad \begin{cases} \tau^\alpha < \tau_c^\alpha \Rightarrow \dot{\gamma}^\alpha = 0; \\ \tau^\alpha = \tau_c^\alpha \Rightarrow \dot{\gamma}^\alpha \geq 0, \end{cases} \tag{37}$$

where τ^α is computed in terms of $\boldsymbol{\sigma}$ and $\mathbf{R}^\alpha$ according to:

$$\forall \alpha = 1, ..., 24: \quad \tau^\alpha = \boldsymbol{\sigma} : \mathbf{R}^\alpha. \tag{38}$$

Eq. (36) can be equivalently expressed as non-linear complementarity problem (NLCP):

$$\forall \alpha = 1, ..., 24: \quad \chi^\alpha = \tau_c^\alpha - \tau^\alpha \geq 0 \quad ; \quad \dot{\gamma}^\alpha \geq 0 \quad ; \quad \chi^\alpha \dot{\gamma}^\alpha = 0. \tag{39}$$

The critical shear stress τ_c^α has as initial value τ_0, and evolves with slip accumulation on the crystallographic systems according to the following generic hardening law:

$$\forall \alpha = 1, ..., 12: \quad \dot{\tau}_c^\alpha = \dot{\tau}_c^{\alpha+12} = \sum_{\beta=1}^{12} H^{\alpha\beta} \left(\dot{\gamma}^\beta + \dot{\gamma}^{\beta+12} \right), \tag{40}$$

where $H^{\alpha\beta}$ is the $\alpha\beta$ component of the hardening matrix $\mathbf{H}$, which is dependent on the accumulated slips of the different slip systems γ^α and some hardening parameters. The explicit expression of the hardening matrix used in the present investigation will be given in Section 5. The single crystal constitutive equations presented here are solved by an explicit integration scheme, whose numerical details are not provided in the present work for the sake of brevity. Readers interested in these numerical details are referred to Akpama et al. (2016).

4. Prediction of ductile failure initiation

In the current study, the strain-based void coalescence criterion developed in Koplik and Needleman (1988) and the Rice bifurcation approach (Rudnicki and Rice, 1975) are respectively adopted to predict the onset of void coalescence and plastic strain localization. As stated by Koplik and Needleman (1988), void coalescence arises at the moment when the strain state shifts from a general triaxial state to a uniaxial strain mode. Within the convention adopted here, this condition is met when the strain rate components in the second and third directions become equal to zero:

$$\dot{E}_{22} = \dot{E}_{33} = 0. \tag{41}$$

Interested readers are referred to Koplik and Needleman (1988) who provide sufficient details about the physical foundation of this criterion.

The present section focuses on the application of the Rice bifurcation theory to predict the onset of plastic strain localization. The

formulation of the corresponding bifurcation criterion depends on the loading state to which the unit cell is subjected. For the sake of clarity, the two loading cases will be separately treated: proportional triaxial stress paths in Section 4.1 and proportional in-plane strain paths in Section 4.2.

4.1. *Bifurcation analysis under proportional triaxial stress paths*

Following the Rice approach, the onset of strain localization is marked by a bifurcation associated with admissible jumps for strain and stress rates through a discontinuity band (Fig. 3). In a Lagrangian framework, the kinematic condition for the strain rate jump reads:

$$[[\dot{\mathbf{F}}]] = \dot{\mathbf{F}}^{O} - \dot{\mathbf{F}}^{I} = \overrightarrow{\dot{\mathscr{C}}}_0 \otimes \overrightarrow{\mathscr{N}}_0, \tag{42}$$

where:

- $[[\dot{\mathbf{F}}]]$ is the jump of $\dot{\mathbf{F}}$ across the localization band, which is equal to the difference between the velocity gradient outside the band $\dot{\mathbf{F}}^{O}$ and its counterpart inside the band $\dot{\mathbf{F}}^{I}$,
- $\overrightarrow{\dot{\mathscr{C}}}_0$ is the jump vector,
- $\overrightarrow{\mathscr{N}}_0$ is the unit vector normal to the localization band in the initial configuration, equal to $(\sin\theta_2\cos\theta_1,\ \sin\theta_2\sin\theta_1,\ \cos\theta_2)$, where $0 \leq \theta_1 \leq 2\pi$ and $0 \leq \theta_2 \leq \pi$.

The condition of force equilibrium through the band writes:

$$[[\dot{\mathbf{P}}]] \cdot \overrightarrow{\mathscr{N}}_0 = \overrightarrow{\mathbf{0}}. \tag{43}$$

The macroscopic tensors $\dot{\mathbf{F}}$ and $\dot{\mathbf{P}}$ are related by the macroscopic tangent modulus $\mathbb{B}$:

$$\dot{\mathbf{P}} = \mathbb{B} : \dot{\mathbf{F}}. \tag{44}$$

By combining Eqs. (41), (42), and (43), one can determine the following expression of jump kinematic condition:

$$\left(\mathbb{B} : \left(\overrightarrow{\dot{\mathscr{C}}}_0 \otimes \overrightarrow{\mathscr{N}}_0\right)\right) \cdot \overrightarrow{\mathscr{N}}_0 = \overrightarrow{\mathbf{0}}, \tag{45}$$

which can be equivalently expressed in index form:

$$\left(\mathscr{N}_{0j} B_{ijkl} \mathscr{N}_{0l}\right) \dot{\mathscr{C}}_{0k} = 0. \tag{46}$$

By introducing the fourth-order tensor $\mathbb{L}$, which is obtained from tensor $\mathbb{B}$ by permutating the first two indices ($\forall i,j,k,l : 1,2,3 : L_{ijkl} = B_{jikl}$), Eq. (45) can be transformed into:

$$\left(\mathscr{N}_{0i} L_{ijkl} \mathscr{N}_{0l}\right) \dot{\mathscr{C}}_{0k} = 0, \tag{47}$$

which is expressed in its vector form as:

$$\left(\overrightarrow{\mathscr{N}}_0 \cdot \mathbb{L} \cdot \overrightarrow{\mathscr{N}}_0\right) \cdot \overrightarrow{\dot{\mathscr{C}}}_0 = \overrightarrow{\mathbf{0}}. \tag{48}$$

Hence, the bifurcation criterion is associated with the singularity of tensor $\overrightarrow{\mathscr{N}}_0 \cdot \mathbb{L} \cdot \overrightarrow{\mathscr{N}}_0$:

$$\det\left(\overrightarrow{\mathscr{N}}_0 \cdot \mathbb{L} \cdot \overrightarrow{\mathscr{N}}_0\right) = 0. \tag{49}$$

The numerical detection of plastic strain localization with the bifurcation criterion given by Eq. (48) can be viewed as a minimization problem:

$$\text{minimize } \det\left(\overrightarrow{\mathscr{N}}_0 \cdot \mathbb{L} \cdot \overrightarrow{\mathscr{N}}_0\right) \text{ for } 0 \leq \theta_1 \leq 2\pi \text{ and } 0 \leq \theta_2 \leq \pi. \tag{50}$$

In the case where the minimum of the determinant of $\overrightarrow{\mathscr{N}}_0 \cdot \mathbb{L} \cdot \overrightarrow{\mathscr{N}}_0$ over all the band orientations (θ_1, θ_2) is strictly positive, there is no localization. Otherwise, plastic strain localization occurs when the minimum of $\det(\overrightarrow{\mathscr{N}}_0 \cdot \mathbb{L} \cdot \overrightarrow{\mathscr{N}}_0)$ vanishes for the first time.

To check the criterion given by Eq. (48), the macroscopic tangent modulus $\mathbb{B}$ must be computed. This computation is based on the condensation technique originally proposed by Miehe (2003). The practical details about the implementation of this technique in connection with the FE computations performed within ABAQUS are given in Zhu et al. (2022).

Table 1
Elasticity and hardening parameters.

Elasticity		Hardening		
E (GPa)	ν	τ_0 (MPa)	h_0 (MPa/s)	n
65	0.3	40	390	0.184

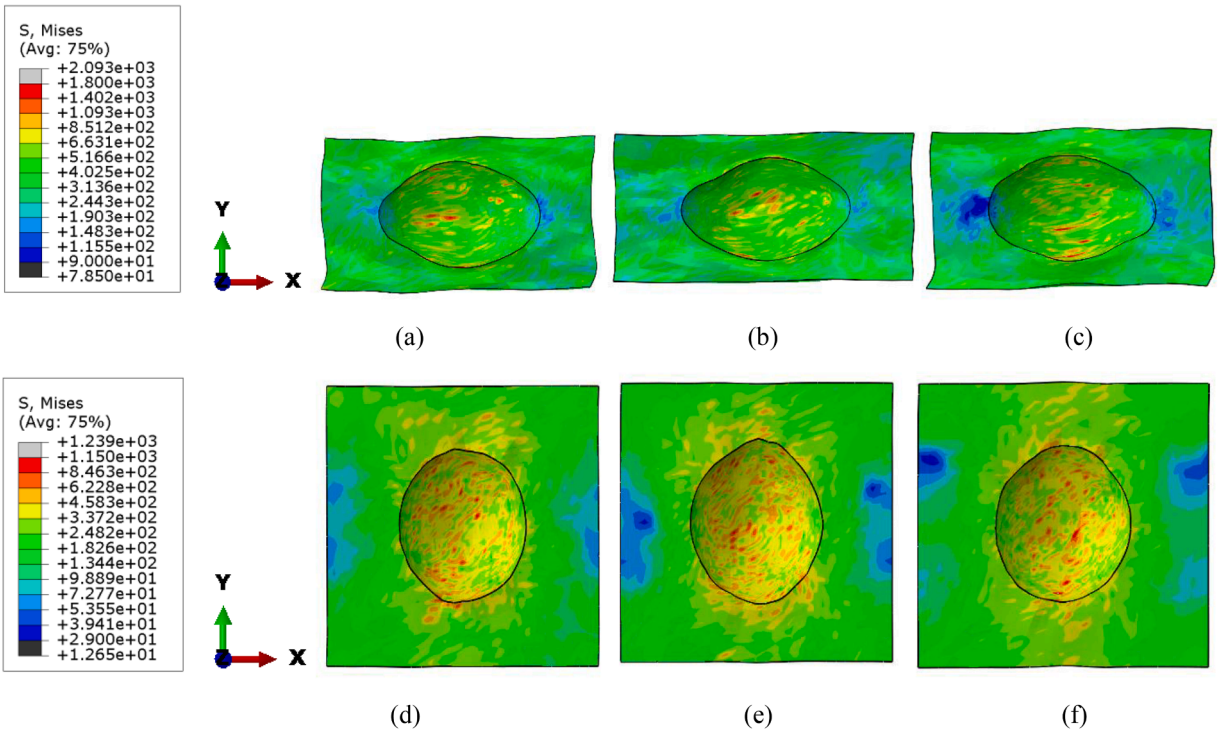

Fig. 4. Effect of triaxiality ratio on the distribution of microscopic von Mises equivalent stress (predicted at the onset of bifurcation): (a) $T = 0.7$, Ran.; (b) $T = 0.7$, Cub.; (c) $T = 0.7$, Cop.; (d) $T = 3$, Ran.; (e) $T = 3$, Cub.; (f) $T = 3$, Cop.

4.2. Bifurcation analysis under proportional in-plane strain paths

Similar to the developments carried out in Section 4.1, in-plane bifurcation occurs when the following condition is satisfied:

$$\det\left({}^{IN}\overrightarrow{\mathscr{N}}_0 \cdot {}^{IN}\mathbb{L} \cdot {}^{IN}\overrightarrow{\mathscr{N}}_0\right) = 0, \tag{51}$$

where ${}^{IN}\mathbb{L}$ is an in-plane tensor related to the in-plane macroscopic tangent modulus ${}^{IN}\mathbb{B}$ by the index relation:

$$\forall i,j,k,l : 1,2 : \quad {}^{IN}L_{ijkl} = {}^{IN}B_{jikl}, \tag{52}$$

and ${}^{IN}\overrightarrow{\mathscr{N}}_0$ is the in-plane unit normal vector (the in-plane form of $\overrightarrow{\mathscr{N}}_0$), equal to $(\cos\theta,\ \sin\theta)$, where $0 \leq \theta \leq \pi/2$.

To apply the bifurcation criterion defined by Eq. (50), the macroscopic in-plane tangent modulus ${}^{IN}\mathbb{B}$ must be evaluated. For this evaluation, the perturbation technique developed in Temizer and Wriggers (2008) is used. The condensation technique presented in Zhu et al. (2022) and used to evaluate the macroscopic tangent modulus for the case of proportional triaxial stressing (see the end of Section 4.1) can be adapted to predict the in-plane tangent modulus ${}^{IN}\mathbb{B}$. However, the perturbation technique seems to be more efficient, when it is applied for proportional in-plane strain paths, than the condensation technique. In fact, for this particular loading, only four linear perturbation steps (and not nine as for a general triaxial loading) are needed to numerically compute the tangent modulus. Therefore, the CPU time corresponding to this evaluation is significantly reduced.

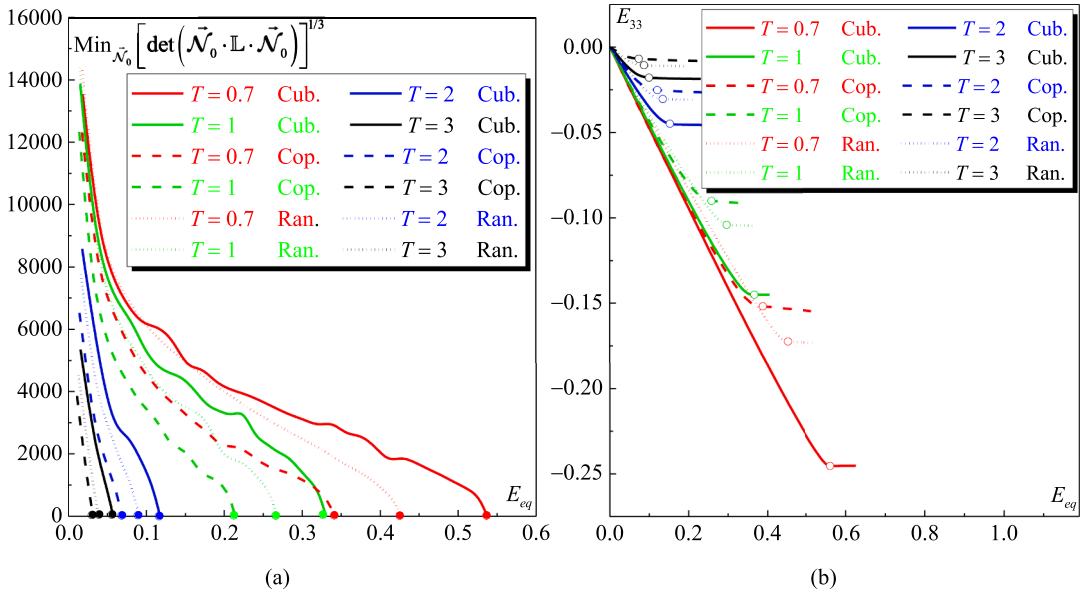

Fig. 5. Impact of the triaxiality ratio on the evolution of the: (a) cubic root of the minimum of $\det(\overrightarrow{\mathcal{N}}_0\cdot\mathbb{L}\cdot\overrightarrow{\mathcal{N}}_0)$; (b) macroscopic strain component E_{33}.

5. Numerical results

5.1. Hardening parameters

For all the crystallographic slip systems, the initial critical shear stress is assumed to be the same and equal to τ_0. The evolution of the critical shear stresses is defined by a power-law hardening model, where the components of the interaction-hardening matrix **H** are given as follows (similar to the hardening matrix used in Yoshida and Kuroda (2012):

$$\forall\,\alpha,\beta=1,\ldots,N_s:\quad H^{\alpha\beta}=h_0\left(1+\frac{h_0\,\Gamma}{\tau_0\,n}\right)^{n-1}\quad;\quad\Gamma=\sum_{\alpha=1}^{2N_s}\gamma^{\alpha}. \tag{53}$$

The components of **H** are identical, as the hardening is assumed to be isotropic. In Eq (56), h_0 and n are hardening parameters, while Γ is the accumulated slip on all the crystallographic slip systems, equal to $\sum_{k=1}^{2N_s}\gamma^k$. The material parameters used in the simulations are listed in Table 1.

5.2. Proportional stress paths

5.2.1. Effect of triaxiality ratio

Classical investigations have clearly revealed the effect of the triaxiality ratio on the void growth and consequently on ductile failure. In the current section, this effect is carefully explored on the basis of several predictions performed by the developed CPFEM-based tool. Firstly, the impact of the triaxiality ratio on the distribution of the microscopic mechanical state and void shape is analyzed. In this aim, the isovalues of the microscopic von Mises equivalent stress, determined when bifurcation is attained, are displayed in Fig. 4 where two extreme triaxiality values are considered: $T=0.7$ and 3 with Lode parameter $L=-1$ for these simulations. The first triaxiality ratio ($T=0.7$) corresponds to an axisymmetric tension stress state ($\Sigma_{11}=3.72\Sigma_{22}\;;\;\Sigma_{22}=\Sigma_{33}$), a triaxiality ratio lower than 0.7 may lead to void collapse. However, the second one ($T=3$) corresponds to a triaxial tension state where the stress components have the same order of magnitude ($\Sigma_{11}=1.37\Sigma_{22}\;;\;\Sigma_{22}=\Sigma_{33}$), which can typically be observed in front of crack tips. These isovalues are obtained using the three crystallographic textures presented in Fig. 2 (namely, 'Ran.', 'Cub.' and 'Cop.' textures). Based on the observations in Fig. 4, two main conclusions can be drawn:

- The strong heterogeneity of the microscopic stress is clearly observed. This heterogeneity reflects well the discontinuity of the microscopic mechanical behavior induced by crystallographic orientations. In fact, two neighbor grains are initially oriented differently. Therefore, the activity of slip systems may significantly differ between these two grains, even if the strain state is almost the same. This difference leads to a remarkable deviation between the microscopic stresses in both grains and a strong heterogeneity in the stress distribution. This point will be better discussed in Section 5.2.3.
- The final void shape (at the onset of bifurcation) is closely correlated to the triaxiality level. Indeed, for the first row of figures (a–c), the triaxiality ratio T is equal to 0.7 leading to an evident elongation along the primary loading direction. This stress

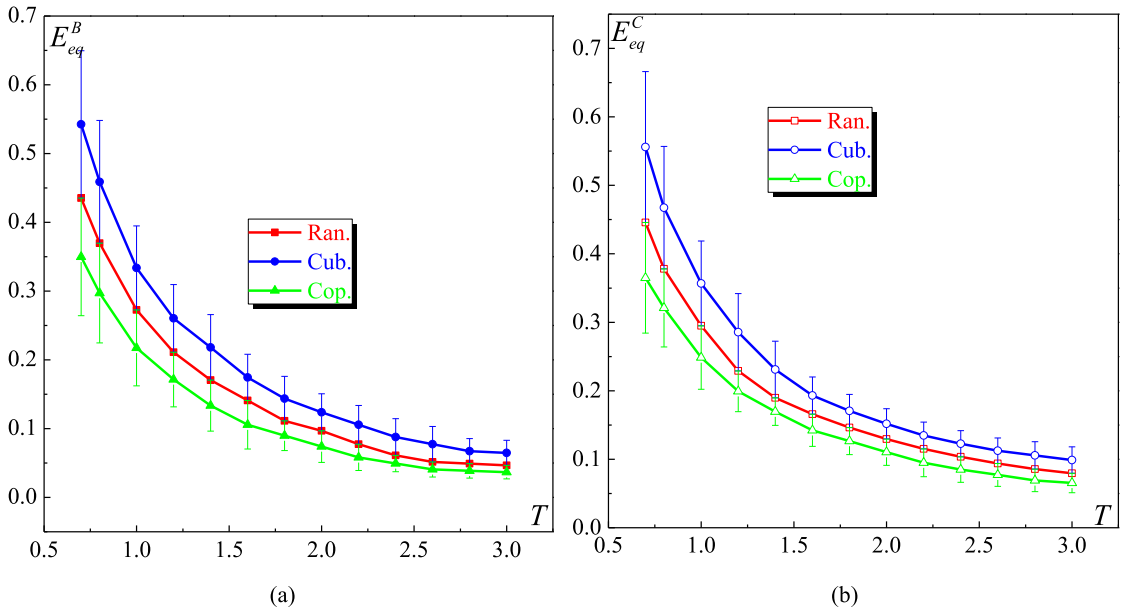

Fig. 6. Influence of the triaxiality ratio on the evolution of the: (a) bifurcation limit strain E^B_{eq}; (b) coalescence limit strain E^C_{eq}.

state justifies the elongated shape of the void at bifurcation. For the second row (d–f), the triaxiality ratio is set to 3, implying a triaxial stress state where the three principal stress components have approximately the same values. Consequently, the void grows in almost homothetic way without significant change of its shape.

The impact of the triaxiality ratio on the two ductility limit indicators is depicted in Fig. 5, where the evolution of the cubic root of the minimum of $\det(\overrightarrow{\mathscr{N}}_0 \cdot \mathbb{L} \cdot \overrightarrow{\mathscr{N}}_0)$ and the macroscopic strain component E_{33} are plotted in Fig. 5a and b, respectively, as functions of the macroscopic (von Mises) equivalent strain E_{eq}. Four proportional triaxial stress states are considered: $T = 0.7$, 1, 2, and 3 with $L = -1$. The macroscopic strain localization is marked by the singularity of the acoustic tensor (see Section 4.1). However, void coalescence is detected when the straining mode switches from a triaxial state to uniaxial state; namely, coalescence happens when the component E_{33} stops decreasing. The critical strains determined by the bifurcation (resp., the void coalescence) criterion E^B_{eq} (resp., E^C_{eq}) are marked by full (resp., open) circles in Fig. 5a (resp., b). It is observed from Fig. 5 that for all the studied loadings, the ductility limit decreases as the triaxiality ratio increases. Furthermore, the ductility limit is reached at realistic strain levels even for low triaxiality ratios. The latter result is partially due to the presence of void, which plays a destabilizing role thus promoting the acceleration of failure occurrence. The void effect will be further discussed in Section 5.2.4. Additionally, the initial crystallographic texture has an important impact on the ductility limit predictions. Such an influence is obvious due to the fact that the difference in crystallographic textures leads to different slip activities, thus implying quite distinct microscopic and macroscopic responses. Such differences naturally impact the void growth and consequently ductile failure. Particularly, Cop. texture leads to the earliest failure, followed by Ran. and then Cub. texture.

To further explore the combined effect of triaxiality ratio and initial crystallographic texture on the ductility limit predictions, the evolutions of the limit strains E^B_{eq} and E^C_{eq} are plotted in Fig. 6 under stress states ranging from $T = 0.7$ to $T = 3$. As we can see, E^B_{eq} and E^C_{eq} decrease with increasing T, regardless of the initial crystallographic texture. Moreover, for a given triaxiality level, the Cub. texture always yields the highest limit strain, followed by Ran. and then Cop. texture. Furthermore, the impact of the crystallographic texture on E^B_{eq} and E^C_{eq} gradually weakens as the triaxiality ratio T increases, as shown by the absolute error bars of critical strains of Cub. and Cop. texture with respect to the Ran. texture. Specifically, for the highest triaxiality ratio ($T = 3$), the effect of the initial texture becomes relatively small. These observations are consistent with those established in Liu et al. (2021), stating that the impact of the crystallographic texture on void growth (precursor to void coalescence) is negligible when the triaxiality level is high. Close results have been obtained by Guo et al. (2020), where the effect of the crystallographic orientation on void coalescence in porous single crystals (not polycrystalline aggregates as in the current case) has been analyzed. These trends are expectable considering the fact that for FCC crystals used in the present contribution, the hydrostatic microscopic stress increases with macroscopic stress triaxiality. As a result, under high macroscopic triaxiality, the microscopic deviatoric stress influencing the slip activity is similar, but it has less impact on the overall response. This interpretation may also be qualitatively supported by the plastic yield-surface functions for porous single crystals given by Han et al. (2013), where it is revealed that the cross-section of yield surfaces becomes less anisotropic with increasing stress triaxiality. Consequently, the grains with different orientations behave more isotropically under high triaxiality, and the impact of the orientation distribution on void growth significantly decreases. Furthermore, at low triaxiality, plastic strain localization and void coalescence are driven by the plastic behavior of the matrix, where the crystallographic texture has a significant impact on the

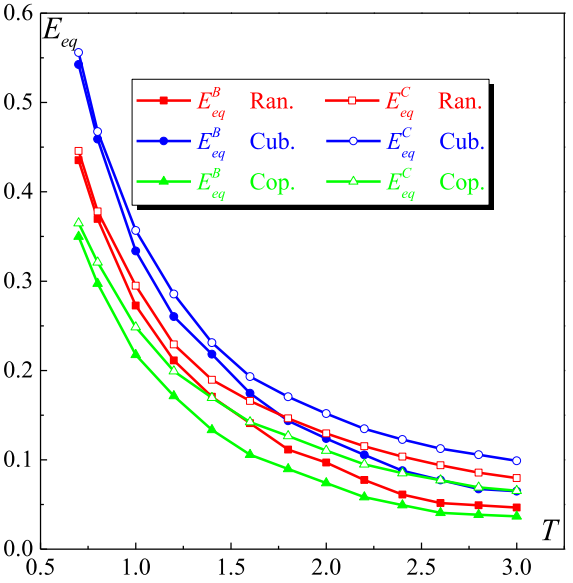

Fig. 7. Effect of the triaxiality ratio on the competition between plastic strain localization and void coalescence.

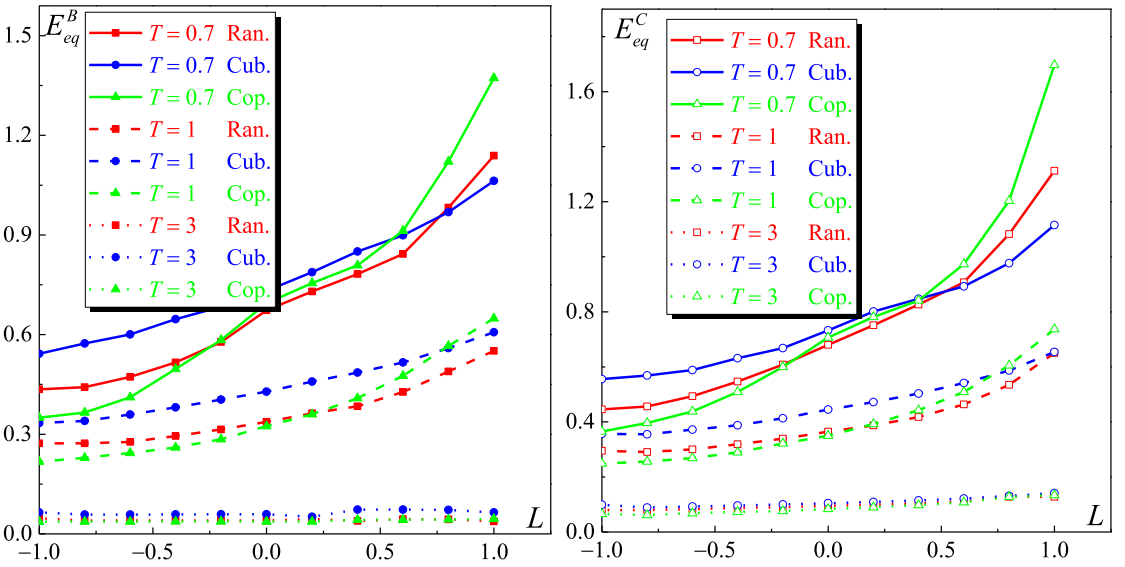

Fig. 8. Impact of the Lode parameter on the evolution of the: (a) bifurcation limit strain E^B_{eq}; (b) coalescence limit strain E^C_{eq}.

evolution of the mechanical state. However, at high stress triaxiality, plastic strain localization and void coalescence strongly rely on the void growth, which evolves exponentially. Hence, in the latter case, the influence of the mechanical behavior of the matrix on the ductility limit becomes small.

As previously stated, several studies have been conducted to investigate the competition between strain localization and void coalescence, such as in Luo and Gao (2018) and Zhu et al. (2020b). In all the above-cited contributions, predictions are performed using phenomenological models, where the dense matrix is commonly presumed to be materially homogeneous and generally isotropic, thus ignoring the microscopic heterogeneity and the strong plastic anisotropy induced by the crystallographic texture. In the present contribution, the combined effect of the triaxiality ratio and crystallographic texture on the competition between plastic strain localization and void coalescence is analyzed, as the unit cell mechanical behavior is modeled by our CPFEM-based strategy. It is observed from Fig. 7 that both phenomena happen almost at the same time for low triaxiality ($T \leq 1$). However, for moderate and high triaxiality levels, macroscopic strain localization occurs prior to void coalescence. Moreover, the discrepancy between the two critical

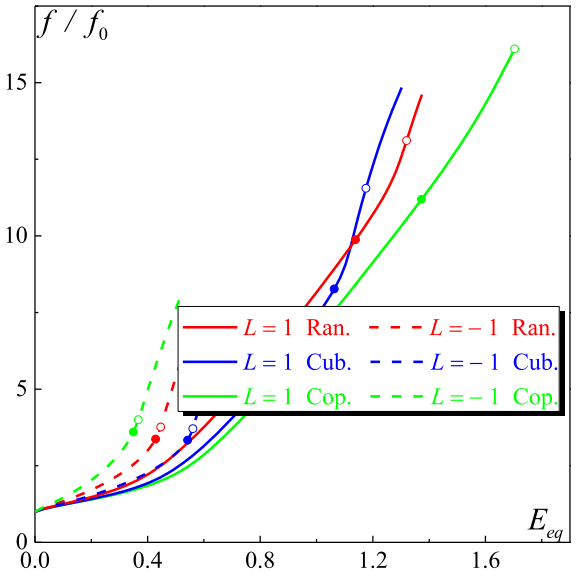

Fig. 9. Impact of the Lode parameter on the void growth evolution defined by the ratio f/f_0.

strains increases as triaxiality ratio T increases. It is noteworthy that these conclusions hold irrespective of the adopted initial crystallographic texture. The conclusions of this competition study are fully consistent with the results obtained in Tekoğlu et al. (2015), where an isotropic phenomenological framework has been adopted to model the mechanical behavior of the matrix material.

5.2.2. Effect of the Lode parameter

Besides the effect of the triaxiality ratio, some studies have revealed, on the basis of experimental evidences (Lode, 1925) and unit cell computations using phenomenological models (Zhang et al., 2001), that the Lode parameter may also significantly influence the void behavior (growth and coalescence). Indeed, different values of the Lode parameter for the same stress triaxiality ratio may result in different limit strains. The objective of the present subsection is to clarify this effect on the evolution of E^B_{eq} and E^C_{eq}, as depicted in Fig. 8a and b, respectively. Three triaxiality ratios are considered in this study: 0.7, 1, and 3. As revealed by this figure, the limit strains increase with the Lode parameter L, which varies from -1 to 1, regardless of the triaxiality ratio level and crystallographic texture. However, the increase rate of the limit strains with parameter L significantly depends on the stress triaxiality ratio T: the larger the value of T, the smaller the influence of L. This result is expected considering the fact that increased triaxiality reduces the effect of the deviatoric part of the macroscopic stress, and consequently the effect of Lode parameter. This observation is consistent with that revealed in previous investigations (see, for instance, Zhu et al., 2020b), where the mechanical behavior of the dense matrix has been described by an isotropic phenomenological model. Combined with the anisotropy effect induced by the crystallographic texture and its evolution, the effect of L reveals to be more interesting to analyze. It is clearly shown in Fig. 8 that the crystallographic texture has weak influence on the ductility limit strains when the triaxiality ratio becomes high. This result confirms once again the trends obtained in Fig. 6, where $L = -1$. Moreover, at relatively low range of L, the limit strain obtained with Cub. texture seems to be the highest, followed by Ran. and Cop. texture. However, this trend changes when L increases, such that the limit strains associated with copper texture become the highest at large values of L. These changing trends may be attributable to the complex effect of the macroscopic Lode parameter on the microscopic behavior, and especially on the activity of crystallographic slip systems.

To better understand the combined effect of L and crystallographic texture on the predicted limit strains, we examine in Fig. 9 the void growth evolutions obtained for two extreme values of L: -1 and 1. The void growth evolution is defined by the ratio between the void volume fraction f and its initial value f_0. For the different predictions, the triaxiality ratio is set to 0.7, thus leading to a strong dependency of the limit strains on the Lode parameter, as shown in Fig. 8. It can be seen from Fig. 9 that for both values of L, the normalized void volume fraction increases exponentially with the applied loading. Moreover, it is evidenced that the void growth increases more quickly when $L = -1$. This result explains why the ductility limits are reached earlier for the loading states corresponding to $L = -1$. Furthermore, void coalescence and plastic strain localization take place almost simultaneously when $L = -1$. However, bifurcation occurs before void coalescence when $L = 1$. For both loading states, the void growth rate and ductility limit strongly depend on the initial crystallographic texture.

5.2.3. Effect of the matrix polycrystallinity

Obviously, the matrix polycrystallinity is expected to affect the void growth behavior and the incipience of plastic strain localization. The effect of such heterogeneity induced by the distribution of crystallographic orientations on the void growth has been previously clarified in Liu et al. (2021). These authors have shown that the matrix polycrystallinity and its modeling within a crystal plasticity framework result in slower void growth (compared to predictions based on isotropic phenomenological modeling). In the

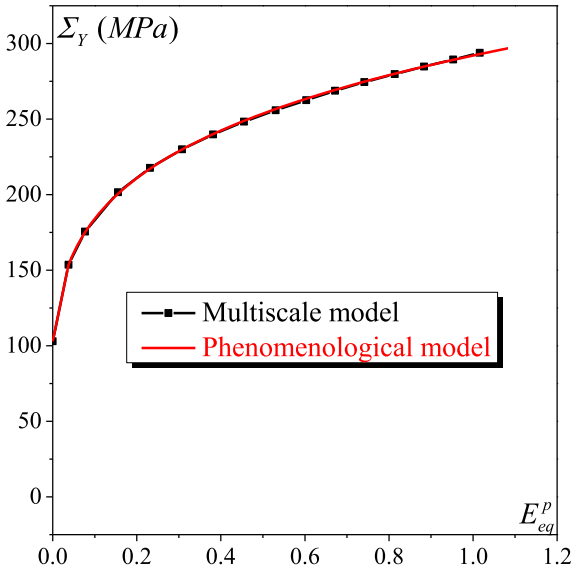

Fig. 10. Identification of the hardening parameters of the phenomenological model.

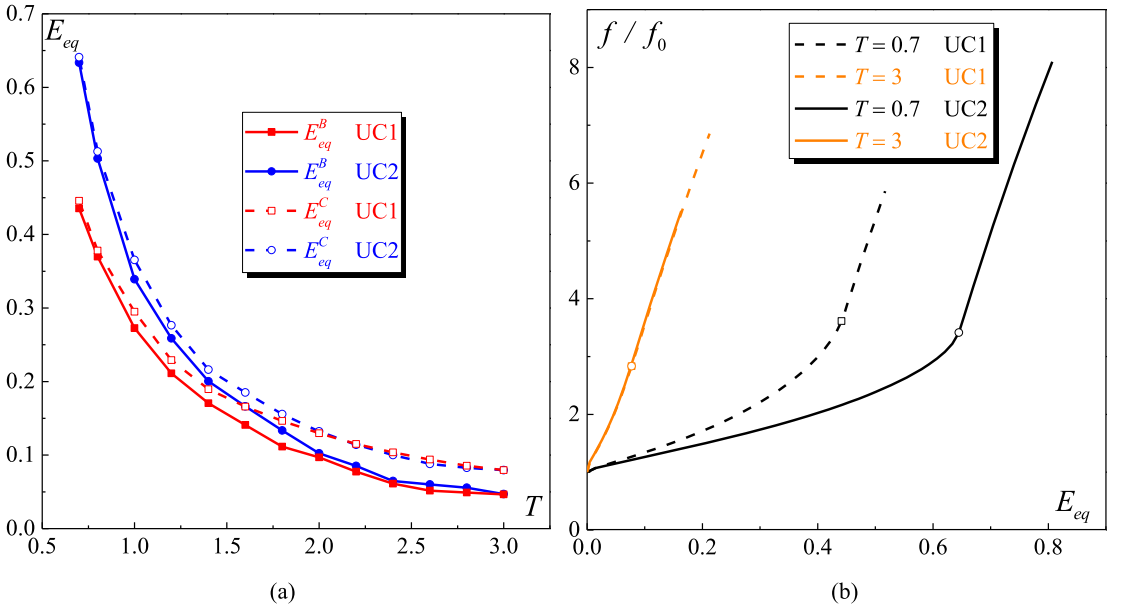

Fig. 11. Impact of the matrix polycrystallinity on ductile failure and void growth: (a) evolution of the limit strains E^B_{eq} and E^C_{eq}; (b) evolution of the void growth defined by the ratio f/f_0.

present investigation, a comparative study is carried out to elucidate the effect of matrix polycrystallinity on the incipience of plastic strain localization and void coalescence. In this aim, two porous unit cells are considered. The first unit cell, referred to hereafter as UC1, is defined by a heterogeneous matrix made of 200 grains. The initial crystallographic orientations of these grains are defined by the Ran. texture shown in Fig. 2a. The second unit cell, briefly called UC2, is defined by a homogeneous matrix. The mechanical behavior of this matrix is modeled within an associative elastoplastic phenomenological framework, where both plasticity and hardening are considered to be isotropic. In this case, the J_2 von Mises criterion is used to model the corresponding yield surface and the isotropic hardening is modeled by the Swift law, where the yield stress Σ_Y is defined in terms of the equivalent plastic strain E^p_{eq}:

$$\Sigma_Y = K\left(E_0 + E^p_{eq}\right)^N, \tag{54}$$

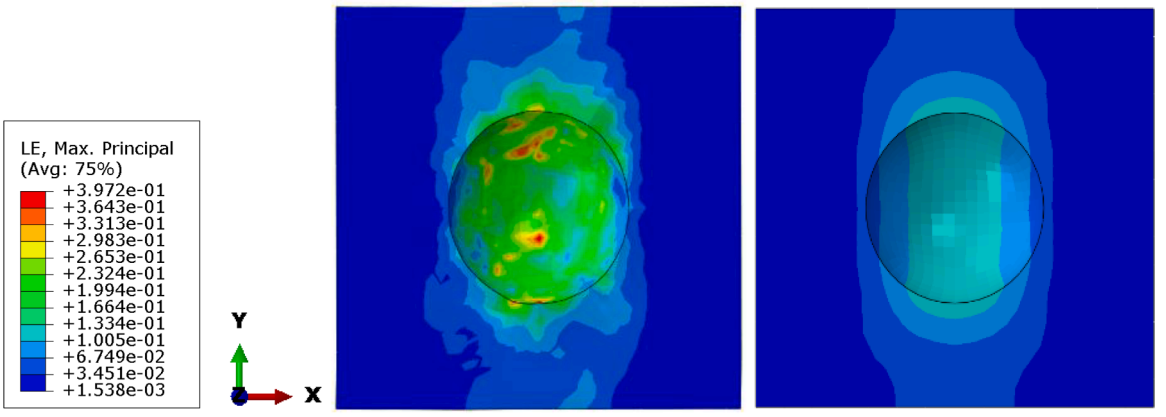

Fig. 12. Impact of the matrix polycrystallinity on the distribution of the microscopic maximum principal strain at $E_{eq} = 0.02$ and $T = 3$: (a) unit cell with polycrystalline matrix; (b) unit cell with homogeneous matrix.

where the hardening parameters K, E_0, and N are calibrated using a numerical uniaxial tensile test applied to a non-porous polycrystalline aggregate made of 200 grains. The Ran. texture presented in Fig. 2a is used to define the initial crystallographic orientations of the grains composing the non-porous polycrystalline aggregate (as this texture leads to the most isotropic behavior compared to the two other ones). On the basis of this identification procedure, the following hardening parameters are obtained:

$$K = 292MPa \quad ; \quad E_0 = 0.0065 \quad ; \quad N = 0.2. \tag{55}$$

The reliability of this identification procedure is illustrated in Fig. 10, where the uniaxial tensile curves determined by both constitutive models (namely, the multiscale and phenomenological models) are almost indistinguishable.

The evolutions of the limit strains E^B_{eq} and E^C_{eq} for UC1 and UC2 against the triaxiality ratio T are presented in Fig. 11a. As we can see, for both unit cells, E^B_{eq} and E^C_{eq} are almost indistinguishable at low stress triaxiality, while their difference increases with increasing the triaxiality ratio T. This is consistent with the trends presented in Section 5.2.1. Meanwhile, this means that the matrix polycrystallinity does not affect the priority between macroscopic void coalescence and strain localization. On the other hand, for each individual limit strain (E^B_{eq} or E^C_{eq}), the difference between the predictions obtained for UC1 and UC2 is found to be large at low triaxiality and negligible at high triaxiality. Specifically, this difference decreases as T increases. This illustrates the fact that the matrix polycrystallinity induced by the random distribution of grain orientations accelerates the ductile failure when the triaxiality ratio is low; however, it does not impact the failure occurrence when the triaxiality is high. The trends obtained at high triaxiality are expectable and consistent with those presented in Liu et al. (2021). In fact, the behavior becomes almost isotropic at high triaxiality, as explained in Section 5.2.1. Therefore, the effect of the matrix polycrystallinity, caused by the random distribution of crystallographic orientations, would be reduced in this case. Consequently, predictions obtained by both the phenomenological and crystal plasticity frameworks are very similar at high triaxiality. However, for low triaxiality, our trends seem to conflict with those provided by Liu et al. (2021), in which they concluded that void growth in homogeneous isotropic matrix is faster than in heterogeneous polycrystals. According to Liu et al. (2021), void coalescence for unit cell with homogeneous matrix would occur earlier, as compared to the case of unit cell with heterogeneous matrix. The difference between the trends obtained in Liu et al. (2021) and those of the current investigation may be attributed to two main facts:

- Firstly, the void used in the unit cell computations performed in Liu et al. (2021) is assumed to be intragranular (i.e., located inside one grain). Hence, the void behavior is strongly dependent on the orientation of the grain containing the void as well as on the orientations of neighboring grains (Liu et al., 2021). By contrast, in the present investigation, intergranular void is considered (i.e., located at the boundary of several grains). Thus, the void behavior in this case is affected by the orientations of all the grains on the surface of the void. This dissimilarity in the void location may explain the difference between the trends obtained in Liu et al. (2021) and our predictions.
- Secondly, in Liu et al. (2021), crystal plasticity is modeled by a rate-dependent framework. Within this framework, macroscopic bifurcation cannot occur if the unit cell is non-porous (as the instantaneous microscopic tangent modulus is only governed by elasticity). Unlike this, a rate-independent framework is used in the current investigation, where the microscopic flow rule is modeled by the classical Schmid law involving a vertex-like yield surface. Consequently, as will be demonstrated in Section 5.2.4, macroscopic bifurcation can be reached even if the unit cell is non-porous. Hence, one can expect that bifurcation occurs faster in a porous unit cell within a rate-independent framework than in a unit cell within a rate-dependent framework. As the bifurcation occurrence is generally precursor to void coalescence, one can presume that the use of rate-independent crystal plasticity in the modeling of the matrix behavior, instead of the classical rate-dependent modeling,

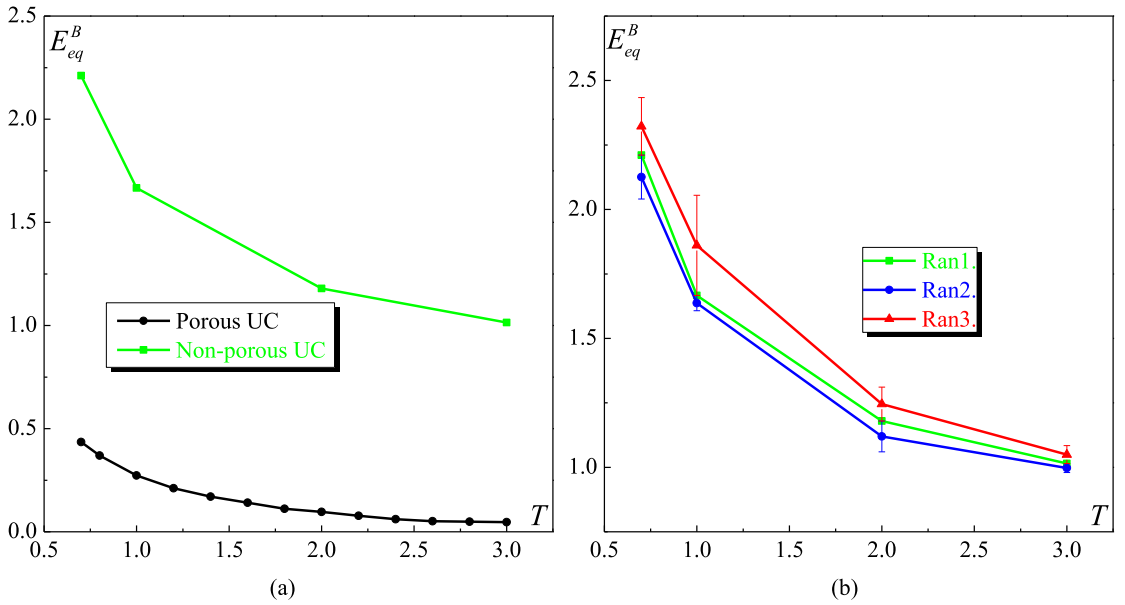

Fig. 13. (a) Impact of the void on the bifurcation limit strain E^B_{eq}; (b) effect of the distribution of crystallographic orientations on the bifurcation limit strain E^B_{eq}.

leads to acceleration of void coalescence. This may explain the difference between our predictions and those obtained in Liu et al. (2021).

To further apprehend the impact of matrix polycrystallinity on the ductility limit, the void growth evolutions are plotted in Fig. 11b for $T = 0.7$ and 3. As can be seen, the void growth in the polycrystalline aggregate is much faster than that in the equivalent homogeneous matrix at $T = 0.7$. However, the effect of matrix polycrystallinity on the void growth seems to be negligibly small for $T = 3$. This result explains the fact that the ductility limits, predicted at low triaxiality by both ductility criteria, are reached earlier in the polycrystalline aggregate, as compared to the equivalent homogeneous matrix, and also the fact that the matrix polycrystallinity effect on the ductility limits decreases as the triaxiality ratio T increases.

Attention is paid in Fig. 12 to the distribution of the microscopic maximum principal strain in the polycrystalline matrix (Fig. 12a) and in the equivalent homogeneous matrix (Fig. 12b) at $E_{eq} = 0.02$ and $T = 3$. The isovalues shown in Fig. 12 highlight the strong heterogeneity of the maximum principal strain distribution observed in the polycrystalline matrix, as compared to the matrix described by a phenomenological model where the studied strain component is more smoothly distributed. This strong heterogeneity is the result of the distribution and evolution of the crystallographic orientations of the polycrystalline aggregate that compose the dense matrix of the unit cell.

5.2.4. Effect of the void and the spatial distribution of crystallographic orientations

The current section is focused on investigating two additional effects on the aggregate ductility limits: the presence of a void at the center of the unit cell and the spatial distribution of crystallographic orientations.

- As we have extensively shown in the previous sections, the void has a strong effect on the failure of porous unit cells. To further investigate this effect, a series of simulations are conducted on non-porous unit cells made of 200 grains, where the crystallographic orientations are defined by the Ran. texture shown in Fig. 2a. On the basis of these predictions, it is observed that bifurcation can be reached but at high strain level, as shown in Fig. 13a. Bifurcation is predicted because the Schmid law is adopted to model the single crystal flow rule. It is well known that the Schmid law, with its vertex-type destabilizing effect, promotes the occurrence of bifurcation at the single crystal level and then at the polycrystalline level. Such bifurcation cannot be predicted if the non-porous unit cell is made of homogeneous material modeled within a phenomenological framework or heterogeneous material modeled within a crystal plasticity rate-dependent framework. Fig. 13a also highlights the effect of the void on the drastic reduction of the bifurcation limit strain. This result is obvious due to the fact that such void acts as defect triggering the initiation of bifurcation.
- One of the major advantages of the CPFEM-based model developed in the present investigation, compared to more classical mean field approaches (for instance, the Taylor model and the self-consistent approach), is its ability to consider the heterogeneity of mechanical fields inside the grain and the effect of grain spatial distribution on the macroscopic mechanical behavior and ductile failure. To illustrate the second effect, let us consider three unit cells made of 200 grains. The Ran. texture shown in Fig. 2a is used for the first unit cell as well as for the two other ones, but the initial crystallographic

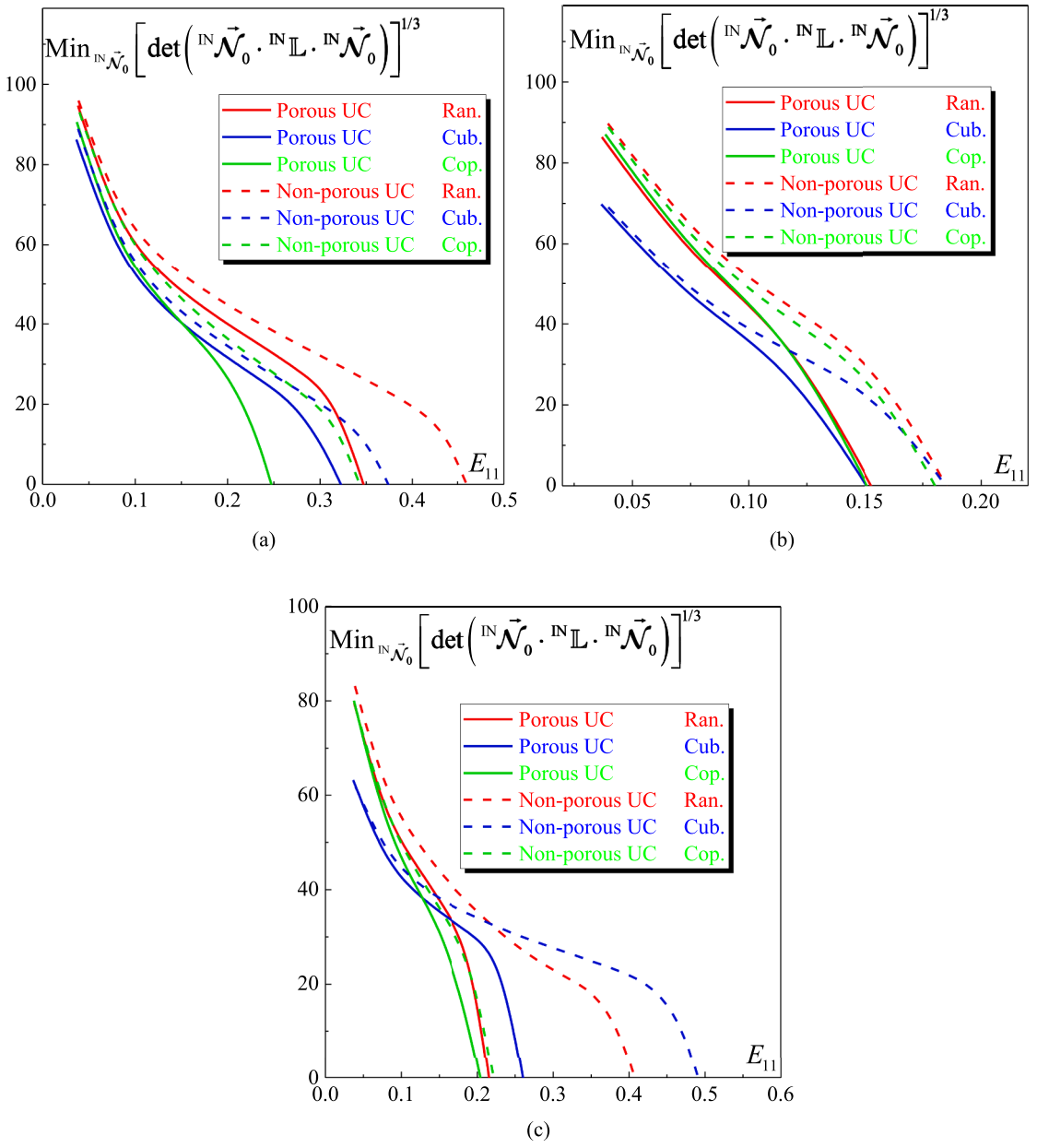

Fig. 14. Impact of the void and initial crystallographic texture on the: evolution of the cubic root of the minimum of the determinant of ${}^{IN}\overrightarrow{\mathcal{N}}_0 \cdot {}^{IN}\mathbb{L} \cdot {}^{IN}\overrightarrow{\mathcal{N}}_0$ for: (a) $\rho = -0.5$; (b) $\rho = 0$; (c) $\rho = 0.4$.

orientations are differently assigned to the grains composing the latter unit cells. The effect of the specific assignment of crystallographic orientations on the bifurcation limit strains is depicted in Fig. 13b, where Ran1., Ran2., and Ran3. textures are used to refer to the different orientation assignments. This figure highlights a non-negligible impact of the orientation distribution on the predicted limit strains, as shown by the absolute error bars with respect to Ran1. texture.

5.3. Proportional in-plane strain paths

Similar to the investigations performed in Zhu et al. (2020b) based on phenomenological models, we have observed in the current study that void coalescence cannot be reached when the unit cells are subjected to proportional in-plane strain loadings. Accordingly, the ductility limits under these mechanical states will only be predicted by the macroscopic strain localization criterion. These ductility limits will be presented in this section in the form of forming limit diagrams (FLDs). Note that the amount of computations required to the investigation of the formability limit using the CPFEM-based approach is quite substantial. Therefore, for the sake of brevity and to

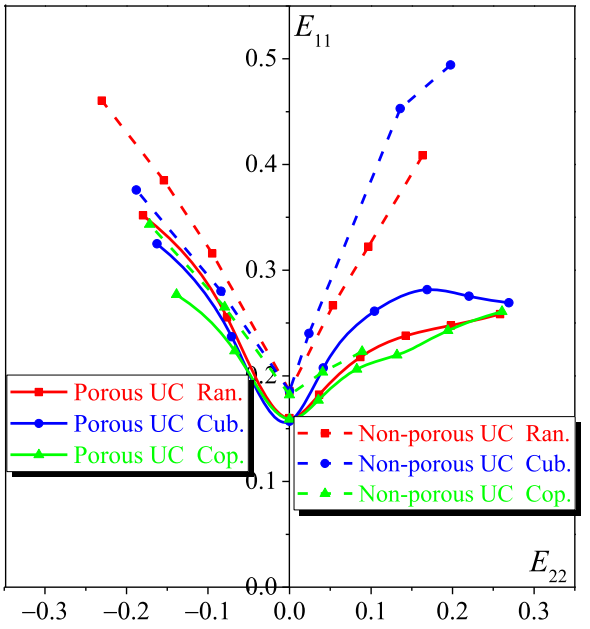

Fig. 15. Impact of the void on the FLDs.

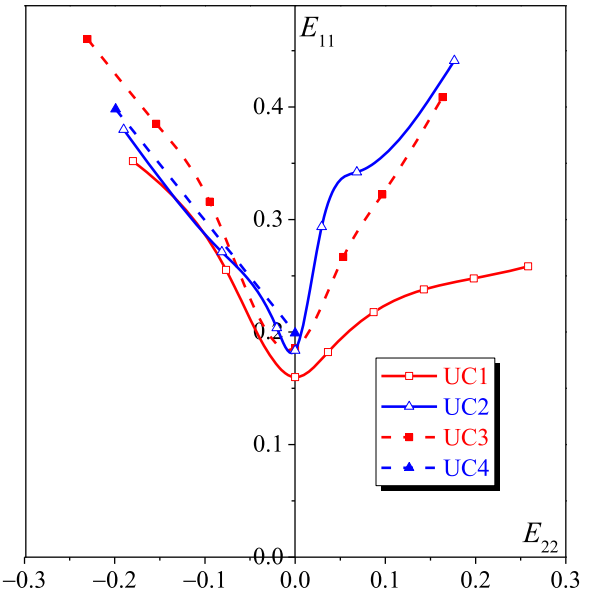

Fig. 16. Combined effect of the void pre-existence and the matrix polycrystallinity on the FLDs.

decrease the computational cost, only some of the representative results will be presented in this section.

5.3.1. Effect of the void

To analyze the combined effect of the pre-existence of void and crystallographic texture on the ductility limits predicted when the unit cell is undergoing proportional in-plane straining, the evolution of the cubic root of the minimum of the determinant of the macroscopic acoustic tensor is plotted in Fig. 14a–c versus the macroscopic strain component E_{11} for three strain paths: $\rho = -0.5$ (uniaxial tension state), $\rho = 0$ (plane-strain tensile state), and $\rho = 0.4$ (biaxial tensile state). From the curves depicted in Fig. 14a–c, the following comments can be made:

- The presence of void considerably reduces the bifurcation limit strain, as compared to the case of non-porous unit cell. This reduction in the limit strain is noticed for all of the considered strain paths and initial crystallographic textures.

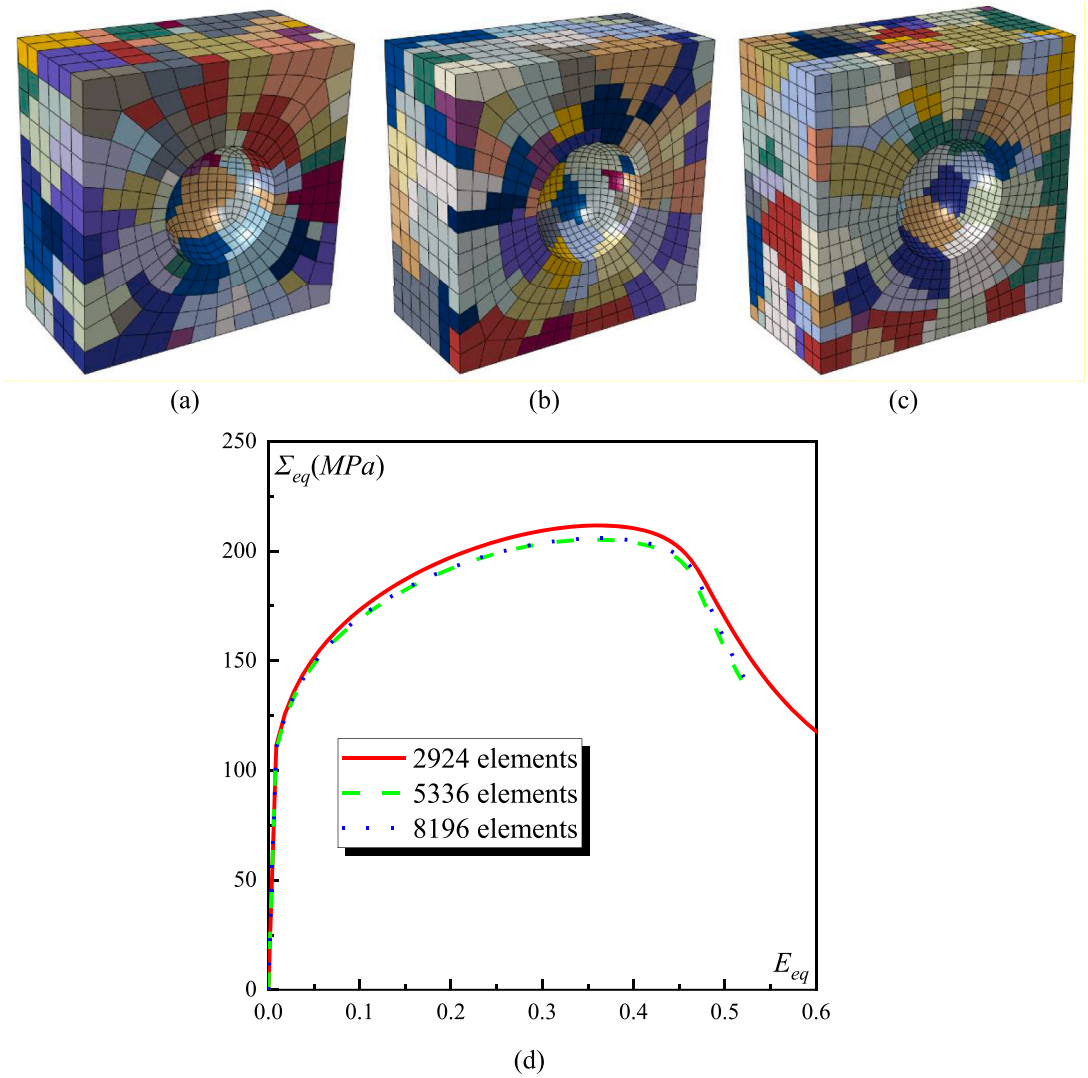

Fig. A.1. Three voided unit cells respectively discretized by: (a) 2924, (b) 5336, and (c) 8196 20-node finite elements. (d) The equivalent von-Mises stress–strain curves corresponding to these three unit cells.

- For the uniaxial tension state ($\rho = -0.5$), the bifurcation limit strain for Ran. texture is the largest, followed by that for Cub. and then Cop. texture (Fig. 14a).
- For the plane-strain tensile state ($\rho = 0$), the bifurcation limit strain shows little dependence on the initial crystallographic texture. For this strain state, bifurcation is reached earlier than for the other strain paths (Fig. 14b).
- For biaxial stretching loading path ($\rho = 0.4$), Cub. texture yields the highest limit strain, followed by Ran. and then Cop. texture (Fig. 14c).

To better illustrate the combined effect of void and crystallographic texture on thin sheet metal formability, FLDs for porous and non-porous unit cells are compared in Fig. 15. From the plots presented in this figure, we clearly observe that the void and crystallographic texture have significant impact on both the level and the shape of the FLDs. For both porous and non-porous unit cells, Ran. texture yields the highest forming limit in the range of negative strain paths ($\rho < 0$). However, Cub. texture provides the highest forming limit in the range of positive strain paths ($\rho > 0$). These texture effects on the forming limits are consistent with what has been shown by Yoshida et al. (2007), where the Taylor-type homogenization approach coupled with the Marciniak–Kuczynski model has been used. Meanwhile, the presence of void reduces the overall level of FLDs, especially for $\rho > 0$. In particular, the ductility reduction for negative strain paths, induced by the presence of void, is more obvious than that observed by Zhu et al. (2020b), where the matrix polycrystallinity has been ignored. It is also found that the presence of void reduces, on the whole, the impact of initial texture on the FLDs. In other words, the differences in forming limits predicted for various textures in porous unit cells are smaller than those in non-porous unit cells.

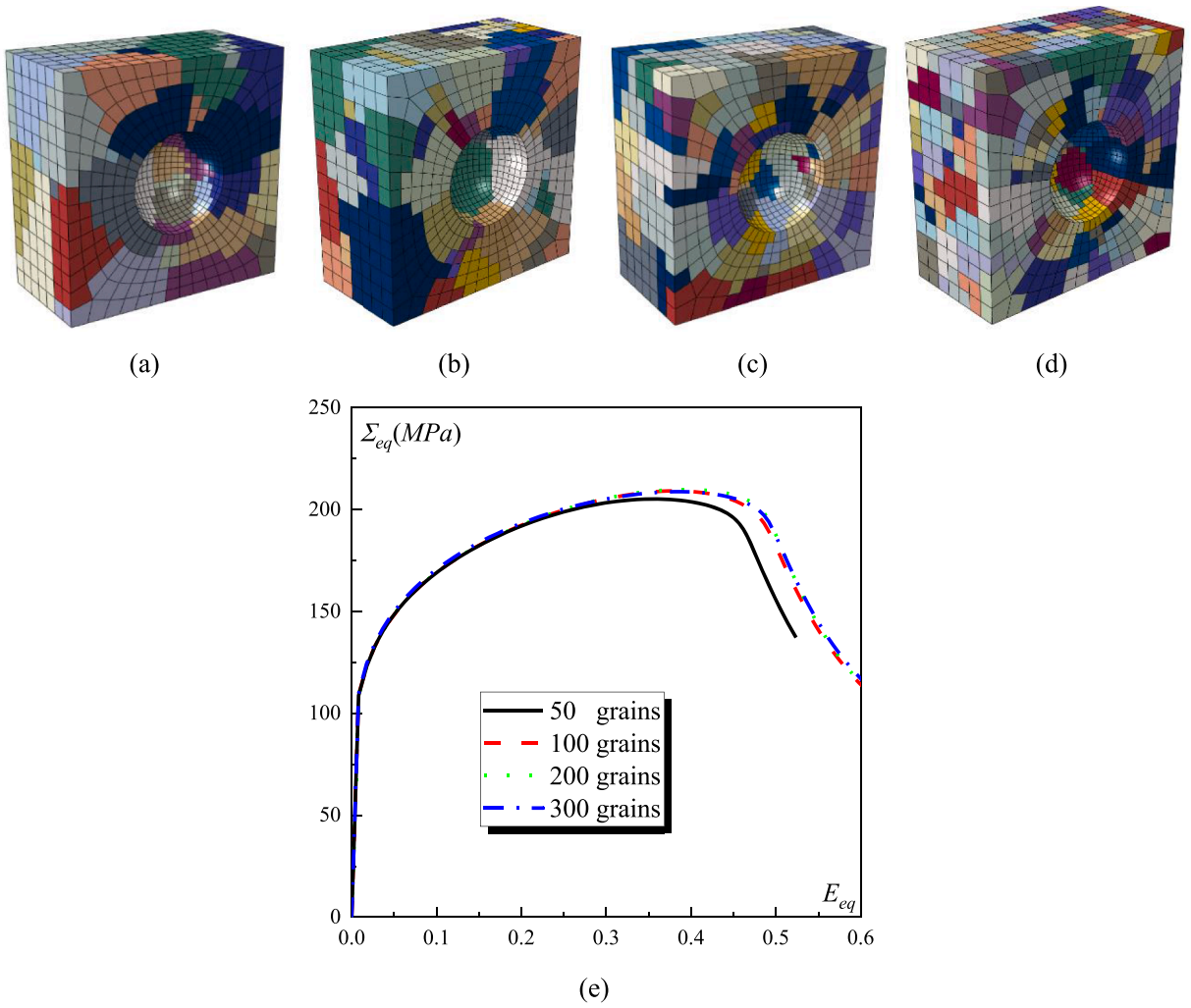

Fig. A.2. The cross section view of voided unit cell containing: (a) 50, (b) 100, (c) 200, and (d) 300 grains. (e) The equivalent von-Mises stress–strain curves corresponding to these four unit cells.

5.3.2. Effect of the matrix polycrystallinity

To illustrate the combined effect of the matrix polycrystallinity and the void on sheet metal formability, let us consider four different unit cells:

- UC1 defined in Section 5.2.3: porous unit cell, where the matrix is assumed to be heterogeneous and made of 200 grains.
- UC2 defined in Section 5.2.3: porous unit cell, where the matrix is assumed to be homogenous with mechanical behavior described by a phenomenological model, as explained in Section 5.2.3.
- UC3: non-porous unit cell made of 200 grains, where a polycrystalline model is used to describe its mechanical behavior. The Ran. texture shown in Fig. 2a is used to define the initial orientations of the grains composing this unit cell. This unit cell is the same as that used in Fig. 13a.
- UC4: non-porous and homogeneous unit cell, whose mechanical behavior is described by the phenomenological model. The associated hardening parameters are defined in Section 5.2.3.

For comparison purposes, the FLDs associated with the different unit cells are plotted in Fig. 16. On the basis of the trends revealed by Fig. 16, the following comments shall be highlighted:

- The limit strains corresponding to UC4 can only be predicted for negative strain paths. Over this strain range, the major strain component E_{11} evolves linearly as a function of the strain-path ratio ρ and is almost equal to $\rho/(1+n)$. For positive strain paths, the ductility limits are reached at unrealistically high strain levels so that the associated limit strains are not shown in

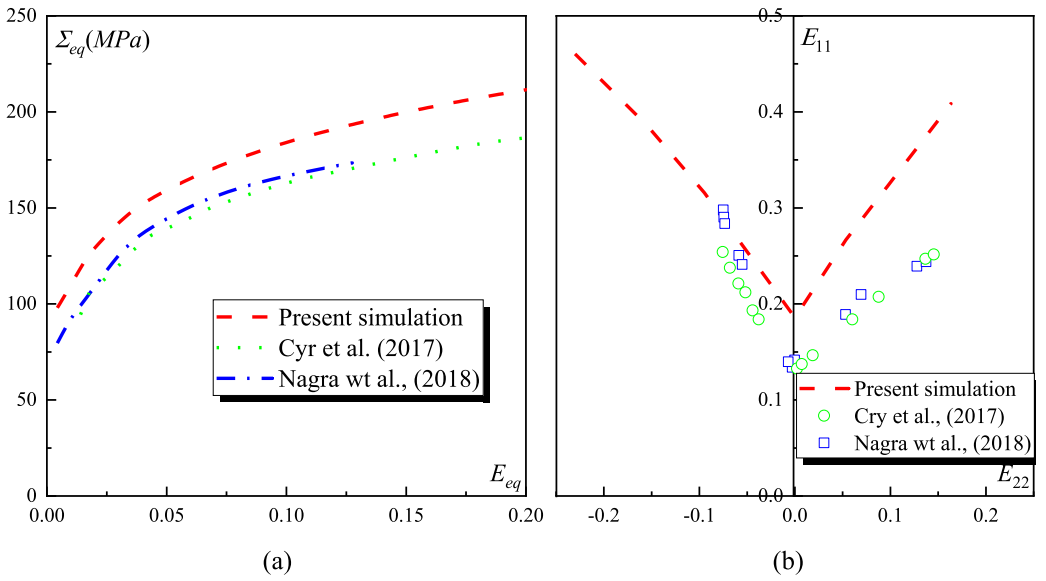

Fig. B.1. Qualitative comparisons between our numerical predictions and experimental data from Cyr et al. (2017) and Nagra et al. (2018): (a) uniaxial tensile stress–strain responses; (b) forming limit diagrams.

Fig. 16. This result is quite anticipated, as a phenomenological model with associative plasticity is adopted to characterize the mechanical behavior of this non-porous unit cell (see, e.g., Ben Bettaieb and Abed-Meraim, 2015).

- For UC3, the limit strains are predicted for the full range of strain paths considered. It is noteworthy that the limit strains are still predicted at realistic levels even for positive strain paths, although the unit cell is non-porous (further details about this point are provided in Appendix B). This result is directly attributed to the use of the Schmid law at the single crystal scale in rate-independent framework, which induces vertex-type destabilizing effects.
- The impact of the void pre-existence on the decrease of the predicted limit strains is obvious, particularly for positive strain paths. For these positive strain paths, the fact that both in-plane strain components E_{11} and E_{22} are positive leads to an increase in the void growth rate, thus accelerating the initiation of bifurcation.

6. Summary and conclusions

In this paper, a new multiscale framework based on CPFEM has been established to accurately predict the mechanical behavior and the ductility limits of polycrystalline aggregates assumed to be statistically representative of thin metal sheets. This framework is based on the periodic homogenization scheme that allows the link between the single crystal and polycrystalline scales. The single crystal constitutive modeling follows a finite strain rate-independent formulation, where the plastic flow is governed by the classical Schmid law. This CPFEM-based framework has been coupled with the bifurcation theory and a void coalescence indicator to predict the ductility limits marked by macroscopic plastic strain localization or void coalescence. To assess the capabilities of the developed tool, two loading configurations have been applied to porous and non-porous aggregates: proportional triaxial stress paths and proportional in-plane strain paths. Various numerical predictions have been carried out to explore the effects of several mechanical and microstructural features on the ductility limits. It is worth emphasizing here the major results obtained through this numerical study:

- The ductility limits induced either by void coalescence or by macroscopic strain localization reveal to be highly dependent on the applied mechanical loading (defined by the triaxiality ratio, the Lode parameter, or the in-plane strain path). The initial crystallographic texture plays an important role in the prediction of ductility limits, especially at low stress triaxiality or positive strain-path ratios.
- Using the current rate-independent CPFEM-based framework, plastic strain localization is predicted at realistic strain levels, even for non-porous polycrystalline aggregates, which is not the case with phenomenological models or rate-dependent crystal plasticity. This result is directly attributed to the use of the Schmid law to model the single crystal flow rule, which induces vertex-type destabilizing effects. The pre-existence of void acts as an additional destabilizing mechanism that promotes the acceleration of ductile failure.
- The use of the proposed CPFEM-based framework allows accounting for the effects of microstructural parameters and features, which cannot be considered by traditional unit cell strategies based on phenomenological constitutive modeling. Disregarding matrix polycrystallinity may lead to overestimation of ductility limit strains, especially in the range of low triaxiality or positive strain-path ratios. Hence, the current CPFEM strategy, which considers the matrix polycrystallinity, allows predicting more realistic ductility limits based on bifurcation theory or void coalescence criterion.

Declaration of Competing Interest

The authors declare that they have no known competing financial interests or personal relationships that could have appeared to influence the work reported in this paper.

Acknowledgments

The authors would like to express their thanks for the financial support from NSFC (12202153).

Appendix A. Sensitivity of the macroscopic behavior to the mesh density and number of grains

To analyze the sensitivity of the numerical predictions to the mesh discretization, we have compared the homogenized stress–strain curves of three voided unit cells discretized by 2924, 5336, and 8196 20-node finite elements, as shown in Fig. A.1a, b and c, respectively. Each unit cell contains 200 grains which are randomly oriented. As clearly shown in Fig. A.1d, the mesh with 5336 finite elements (the same as that used in this work) is sufficient to obtain accurate numerical predictions.

Regarding the representativeness of grain number, we have conducted a grain number sensitivity study. For this purpose, we have compared the homogenized stress–strain curves of four spherically voided unit cells containing 50, 100, 200, and 300 grains, as shown by Fig. A.2a, b, c, and d, respectively. A random texture is generated to define the crystallographic orientations of the grains constituting each polycrystalline aggregate. Each unit cell is discretized by 5336 20-node finite elements. As can be seen from Fig. A.2e, the grain number can affect the stress–strain response unless more than 100 grains are used. In other words, the unit cell containing 200 grains is indeed representative of the studied polycrystalline materials.

Appendix B. Qualitative comparison between numerical predictions and experimental data

We have stated that the proposed CPFEM-based framework predicts realistic ductility limit strains even if the unit cells are non-porous. This is directly attributed to the use of the classical Schmid law to model the plastic flow at the single crystal scale (without any regularization of the yield surface), which induces vertex-type destabilizing effects. In other words, it is not necessary to introduce an initial geometric or material imperfection (e.g., a void or a groove, as in the Marciniak–Kuczynski approach) into the unit cell for predicting reliable formability limits. To validate this aspect, we have compared in Fig. B.1 our predictions (for non-porous unit cell with initially random grain orientations) with the experimental data from Cyr et al. (2017) and Nagra et al. (2018). As shown in Fig. B.1, the tensile stress–strain curve obtained by our unit cell computations (extracted from Fig. 10) is approximatively 50 *MPa* higher than those obtained by experiments. This means that the material used in our simulations shows higher yield stress, which is responsible for relatively higher forming limit strains than the experimental ones (especially in the range of positive strain paths), as shown by Fig. B.1. Although the comparison is qualitative, it proves that the ductility limit strains predicted by our proposed framework are quite acceptable compared to the experiments. If a rate-dependent crystal plasticity model is used instead of the rate-independent model based on the classical Schmid law, the predicted limit strains will be extremely high, as the microscopic tangent modulus coincides with the elasticity one. Similar difference can be observed if a regularized version of the Schmid law (Paux et al., 2020) is used instead of the classical Schmid law. Therefore, the introduction of destabilizing effects through vertices on the current points of the yield surface is a physical and natural way to considerably decrease the predicted limit strains, and thus to obtain results in the same order of magnitude as the experimental results.

References

ABAQUS, 2014. User's Manual 6.14. Abaqus Inc.

Akpama, H.K., Ben Bettaieb, M., Abed-Meraim, F., 2017. Localized necking predictions based on rate-independent self-consistent polycrystal plasticity: bifurcation analysis versus imperfection approach. Int. J. Plast. 91, 205–237.

Akpama, H.K., Ben Bettaieb, M., Abed-Meraim, F., 2016. Numerical integration of rate-independent BCC single crystal plasticity models: comparative study of two classes of numerical algorithms. Int. J. Numer. Methods Eng. 108, 363–422.

Beausir, B., Fundenberger, J.-J., 2017. Analysis Tools for Electron and X-ray diffraction, ATEX - software. Université de Lorraine - Metz. www.atex-software.eu.

Ben Bettaieb, M., Abed-Meraim, F., 2015. Investigation of localized necking in substrate-supported metal layers: comparison of bifurcation and imperfection analyses. Int. J. Plast. 65, 168–190.

Christodoulou, P.G., Dancette, S., Lebensohn, R.A., Maire, E., Beyerlein, I.J., 2021. Role of crystallographic orientation on intragranular void growth in polycrystalline FCC materials. Int. J. Plast. 147, 103104.

Cyr, E., Mohammadi, M., Brahme, A., Mishra, R.K., Inal, K., 2017. Modeling the formability of aluminum alloys at elevated temperatures using a new thermo-elasto-viscoplastic crystal plasticity framework. Int. J. Mech. Sci. 128–129, 312–325.

De Souza Neto, E.A., Feijóo, R.A., 2010. Variational Foundations of Large Strain Multiscale Solid Constitutive Models: kinematical Formulation. Advanced Computational Materials Modeling: From Classical to Multiä-Scale Techniques, pp. 341–378.

Guo, H.J., Ling, C., Busso, E.P., Zhong, Z., Li, D.F., 2020. Crystal plasticity based investigation of micro-void evolution under multi-axial loading conditions. Int. J. Plast. 129, 102673.

Gurson, A.L., 1977. Continuum theory of ductile rupture by void nucleation and growth: part I—Yield criteria and flow rules for porous ductile media. J. Eng. Mater. Technol. 99, 2–15.

Han, X., Besson, J., Forest, S., Tanguy, B., Bugat, S., 2013. A yield function for single crystals containing voids. Int. J. Solids Struct. 50, 2115–2131.

Hill, R., 1952. On discontinuous plastic states, with special reference to localized necking in thin sheets. J. Mech. Phys. Solids 1, 19–30.

Hosseini, N.J., Nieto-Fuentes, C., Dakshinamurthy, M., Rodríguez-Martínez, J.A., Vadillo, G., 2022. The effect of material orientation on void growth. Int. J. Plast. 148, 103149.
Klawonn, A., Lanser, M., Uran, M., Rheinbach, O., Köhler, S., Schröder, J., Scheunemann, L., Brands, D., Balzani, D., Gandhi, A., Wellein, G., Wittmann, M., Schenk, O., Janalík, R., 2020. Exasteel: towards a virtual laboratory for the multiscale simulation of dual-phase steel using high-performance computing. Lecture Notes in Computational Science and Engineering, pp. 351–404.
Koplik, J., Needleman, A., 1988. Void growth and coalescence in porous plastic solids. Int. J. Solids Struct. 24, 835–853.
Lebensohn, R.A., Escobedo, J.P., Cerreta, E.K., Dennis-Koller, D., Bronkhorst, C.A., Bingert, J.F., 2013. Modeling void growth in polycrystalline materials. Acta Mater 61, 6918–6932.
Lee, C., 2020. Effect of microporosity and loading condition on fatigue life of A356 casting alloys. Mater. Sci. Eng. A 776.
Lee, C., Shin, K., Kim, Y., 2017. Dependence of tensile ductility on damage evolution of eutectic Si-particles and pre-existing micro-voids in Al-Si casting alloy. Eng. Fract. Mech. 175, 339–356.
Lejeunes, S., Bourgeois, S., 2011. Une Toolbox Abaqus pour le calcul de propriétés effectives de milieux hétérogènes. In: 10e Colloque National En Calcul Des Structures. Giens, France, pp. 1–9.
Ling, C., Tanguy, B., Besson, J., Forest, S., Latourte, F., 2017. Void growth and coalescence in triaxial stress fields in irradiated FCC single crystals. J. Nucl. Mater. 492, 157–170.
Liu, J., Huang, M., Li, Z., Zhao, L., Zhu, Y., 2021. Microvoid growth mechanism in FCC polycrystals and a statistical damage model. Int. J. Plast. 137, 102888.
Liu, Z.G., Wong, W.H., Guo, T.F., 2016. Void behaviors from low to high triaxialities: transition from void collapse to void coalescence. Int. J. Plast. 84, 183–202.
Lode, W., 1925. Versuche über den einflub der mittleren hauptspannug auf die fliebgrenze. Zeitschrift für Angew. Math. und Mech. Angew. Math. und Mech. 5, 142–144.
Luo, T., Gao, X., 2018. On the prediction of ductile fracture by void coalescence and strain localization. J. Mech. Phys. Solids 113, 82–104.
Marciniak, Z., Kuczyński, K., 1967. Limit strains in the processes of stretch-forming sheet metal. Int. J. Mech. Sci. 9, 609–620.
Miehe, C., 2003. Computational micro-to-macro transitions for discretized micro-structures of heterogeneous materials at finite strains based on the minimization of averaged incremental energy. Comput. Methods Appl. Mech. Eng. 192, 559–591.
Nagra, J.S., Brahme, A., Mishra, R., Lebensohn, R.A., Inal, K., 2018. An efficient full-field crystal plasticity-based M-K framework to study the effect of 3D microstructural features on the formability of polycrystalline materials. Model. Simul. Mater. Sci. Eng. 26, 75002.
Nasir, M.W., Chalal, H., Abed-Meraim, F., 2021. Formability prediction using bifurcation criteria and GTN damage model. Int. J. Mech. Sci. 191, 106083.
Nemat-Nasser, S., 1999. Averaging theorems in finite deformation plasticity. Mech. Mater. 31, 493–523.
Neil, C.J., Agnew, S.R., 2009. Crystal plasticity-based forming limit prediction for non-cubic metals: application to Mg alloy AZ31B. Int. J. Plast. 25, 379–398.
Paux, J., Ben Bettaieb, M., Badreddine, H., Abed-Meraim, F., Labergere, C., Saanouni, K., 2020. An elasto-plastic self-consistent model for damaged polycrystalline materials: Theoretical formulation and numerical implementation. Comput. Methods Appl. Mech. Eng. 368, 113138.
Raabe, D., Roters, F., 2004. Using texture components in crystal plasticity finite element simulations. Int. J. Plast. 20, 339–361.
Reboul, J., Srivastava, A., Osovski, S., Vadillo, G., 2020. Influence of strain rate sensitivity on localization andvoid coalescence. Int. J. Plast. 125, 265–279.
Rousselier, G., 2021. Porous plasticity revisited: macroscopic and multiscale modeling. Int. J. Plast. 136, 102881.
Rudnicki, J.W., Rice, J.R., 1975. Conditions for the localization of deformation in pressure-sensitive dilatant materials. J. Mech. Phys. Solids 23, 371–394.
Schwindt, C., Schlosser, F., Bertinetti, M.A., Signorelli, J.W., 2015. Experimental and Visco-Plastic Self-consistent evaluation of forming limit diagrams for anisotropic sheet metals: an efficient and robustimplementation of the M-K model. Int. J. Plast. 73, 62–99.
Serenelli, M.J., Bertinetti, M.A., Signorelli, J.W., 2010. Investigation of the dislocation slip assumption on formability of BCC sheet metals. Int. J. Mech. Sci. 52 (12), 1723–1734.
Serenelli, M.J., Bertinetti, M.A., Signorelli, J.W., 2011. Study of limit strains for FCC and BCC sheet metal using polycrystal plasticity. Int. J. Solids. Struct. 48 (7), 1109–1119.
Signorelli, J.W., Bertinetti, M.A., Turner, P.A., 2009. Predictions of forming limit diagrams using a rate-dependent polycrystal self-consistent plasticity model.
Shang, X., Zhang, H., Cui, Z., Fu, M.W., Shao, J., 2020. A multiscale investigation into the effect of grain size on void evolution and ductile fracture: experiments and crystal plasticity modeling. Int. J. Plast. 125, 133–149.
Tekoğlu, C., Hutchinson, J.W., Pardoen, T., 2015. On localization and void coalescence as a precursor to ductile fracture. Philos. Trans. R. Soc. A Math. Phys. Eng. Sci. 373.
Temizer, I., Wriggers, P., 2008. On the computation of the macroscopic tangent for multiscale volumetric homogenization problems. Comput. Methods Appl. Mech. Eng. 198, 495–510.
Thomason, P.F., 1990. Ductile Fracture of Metals. Pergamon, Oxford.
Tvergaard, V., Needleman, A., 1984. Analysis of the cup-cone fracture in a round tensile bar. Acta Metall 32, 157–169.
Yerra, S.K., Tekoğlu, C., Scheyvaerts, F., Delannay, L., Van Houtte, P., Pardoen, T., 2010. Void growth and coalescence in single crystals. Int. J. Solids Struct. 47, 1016–1029.
Yoshida, K., Ishizaka, T., Kuroda, M., Ikawa, S., 2007. The effects of texture on formability of aluminum alloy sheets. Acta Mater 55, 4499–4506.
Yoshida, K., Kuroda, M., 2012. Comparison of bifurcation and imperfection analyses of localized necking in rate-independent polycrystalline sheets. Int. J. Solids Struct. 49, 2073–2084.
Xu, Z., Britton, B., Guo, Y., 2021. Casting voids in nickel superalloy and the mechanical behaviour under room temperature tensile deformation. Mater. Sci. Eng. A 806.
Zhang, K.S., Bai, J.B., François, D., 2001. Numerical analysis of the influence of the Lode parameter on void growth. Int. J. Solids Struct. 38, 5847–5856.
Zhu, J.C., Ben Bettaieb, M., Abed-Meraim, F., 2022. Comparative study of three techniques for the computation of the macroscopic tangent moduli by periodic homogenization scheme. Eng. Comput 38, 1365–1394.
Zhu, J.C., Ben Bettaieb, M., Abed-Meraim, F., 2020a. Numerical investigation of necking in perforated sheets using the periodic homogenization approach. Int. J. Mech. Sci. 166, 105209.
Zhu, J.C., Ben Bettaieb, M., Abed-Meraim, F., 2020b. Investigation of the competition between void coalescence and macroscopic strain localization using the periodic homogenization multiscale scheme. J. Mech. Phys. Solids 143, 104042.